Spring 5-1-2019

Studies on the Generation and Detection of Orbital Angular Momentum Based on Beam-Shaping Techniques

xijie luo

Xijie Luo

Candidate

Physics and Astronomy

Department

This dissertation is approved, and it is acceptable in quality and form for publication:

Approved by the Dissertation Committee:

Francisco Elohim Becerra-Chavez , Chairperson

Keith Lidke

Alejandro Manjavacas

Studies on the Generation and Detection of Orbital Angular Momentum Based on Beam-Shaping Techniques

by

Xijie Luo

B.S., Shanxi University, 2014

THESIS FOR MS

Submitted in Partial Fulfillment of the
Requirements for the Degree of

Master of Science
Physics

The University of New Mexico

Albuquerque, New Mexico

May, 2019

Dedication

To all mindful social builders and contributors.

Your existence have made all my hardworks meaningful.

Acknowledgments

This thesis would have never been possible without all the support from my family, friends, and mentors. Thanks to all the people who helped and supported me during years of studying for my MS.

First and foremost, I would like to express my very great appreciation to my advisor Francisco Elohim Becerra-Chavez, whose profound knowledge and encouragement guided me through the maze of research. Thanks to all the patience and great effort he put to help improve my thesis.

I also thank my committee members, Dr. Keith Lidke and Dr. Alejandro Manjavacas, for their kind and valuable comments on my work. I would like to thank Ivan H. Deutsch who led me to the world of quantum mechanics and quantum optics via his inspiring classes. Thanks, Carl Caves and Akimasa Miyake, who introduced me to the broad field of quantum information and quantum computing.

I would like to offer my special thanks to Gloria Cordova for booking the flights and hotels for SQuInt; Alisa Gibson for keeping me in track of all the paperwork and administration procedures; Gary Harrison and Steve Portillo, who always fixed annoying problems in the lab promptly.

I am particularly grateful for the help given by Andy Ferdinand, who taught me how to troubleshoot the experiment when I started doing research. Nathaniel Ristoff, Matthew DiMario, and Ezequiel Carrasco gave me inspiring suggestions when problems occurred in my experiment. Thanks to Rafael N. Alexander and Travis Shelton, who were very generous to give me advice on doing presentations and academic writing; Xiaodong Qi, who gave me great help during my research years in the CQuIC group and helped me tremendously when I started writing my thesis. Thanks to the rest of current or former CQuIC members who discussed their thoughtful work with me.

I would like to thank my parents, Jun Luo and Shusheng Zhang, for their under-

standing and encouragement for me to finish my study overseas. Thanks Monica Sanchez, Satomi Sugaya, Hanieh Mazloom Farsibaf, Karishma Bansal, Adrian Orozco, Qufei Gu, Zhixian Yu, Lewis Chiang, Nan Li, Ning Hsu, Lei Ma, and Ke Huang, for the frequent gathering times and cheers. Thanks to my lovely roommates Zhu Zhu, Ying Wang, and Yingqi Wang, who treated me like family. Finally, I wish to thank Yichen Gao, Manyun Guo, Xindi Huang, Tianjun Chen, Rujiao Wang, and San Jin, for their years-long friendship with me.

For all the caring people in my life, I would like to thank you for your kindness and love.

Studies on the Generation and Detection of Orbital Angular Momentum Based on Beam-Shaping Techniques

by

Xijie Luo

B.S., Shanxi University, 2014

M.S., Physics, University of New Mexico, 2019

Abstract

Light carrying orbital angular momentum (OAM) has many applications ranging from optical manipulation, imaging and remote sensing, and optical communications, and can be used to perform fundamental studies in quantum mechanics and quantum information. Moreover, single photons with high-order OAM allow for increasing the amount of information carried per photon in quantum communication. This thesis describes the study of methods for the preparation and detection of OAM of light in high mode order by utilizing beam shaping techniques using spatial light modulators (SLMs). The quality of the generated high-order OAM mode is limited by optical aberrations which are induced by optical elements in realistic systems and propagation through realistic channels. In order to create and characterize the OAM modes with high quality, we investigate methods for aberration detection and correction using SLMs. These beam shaping techniques for the correction of optical aberrations allow us to generate and detect light carrying OAM with mode order ranging from $l = 0$ to $l = 8$ with good quality, and to generate high quality superpositions of OAM modes with high mode order or in high dimensions. Furthermore, we observe low crosstalk and good levels of mode discrimination between different OAM modes of

light. Our experimental setup can be applied in future studies to investigate and test different protocols in quantum information with high dimensional systems, such as high dimensional quantum state tomography.

Contents

List of Figures

List of Tables

Chapter 1

Introduction

Photons are ideal carriers of information. Light has different degrees of freedom that can be used for encoding and transmitting information, such as frequency, polarization, and the spatial degree of freedom. In particular, leveraging the spatial degree of freedom of light allows for increasing the amount of information that can be encoded in a single photon. Laguerrre-Gaussian (LG) modes which have a well defined OAM, can be used to decompose the transverse field profile of light, and to define a high-dimensional (multimode) photonic states for investigations in quantum information and communication. In this thesis, we investigate the generation and measurement of states of light carrying OAM, with the goal of demonstrating an experimental setup that can perform state preparation and measurement of OAM states of light with high quality. This setup will be useful for future investigations of quantum state tomography (QST) protocols for the characterization of high-dimensional quantum states of photons.

Light consists of photons, each photon with with energy $\hbar\omega$ and linear momentum $\hbar\vec{k}$. Photons can carry spin and orbital angular momentum. Photon with left circular polarization carries spin angular momentum with an amount of $\hbar$ and with right circular polarization carries spin angular momentum of $-\hbar$ per photon along the propagation direction. Light with OAM has an azimuthal phase dependence $\exp(il\theta)$, where θ is the polar angle of the phase front of light, and each photon in this light

beam contains l units of OAM ($l\hbar$), first recognized by Allen *et al.* [2] in 1992. In 1995, He *et al.* [3] showed it is possible to experimentally observe the transfer of OAM from photons to absorptive particles. This OAM transfer process induced a rotational motion in the particles, showing that the OAM is a physical property contained in the photon, which can be transferred to different systems, not only a mathematical novelty. Beyond OAM transfer between light and matter, the OAM has other applications in optical tweezers for micromechanical or microfluidic control [4], digital imaging [5] and astronomy [6, 7].

Light carrying OAM can be generated in different ways, for example, sending the light through a spiral phase plate [8], a q-plate [9], and using beam shaping techniques based on spatial light modulators (SLMs) [10]. Neshev *et al.* [11] observed experimentally the formation of a robust discrete optical vortex solitons in two-dimensional optically induced photonic lattices. Moreover, there are different processes that can be used to generate correlated light beams and photon pairs carrying OAM. In the spontaneous parametric down-conversion (SPDC) processes, the two generated photons are entangled with OAM [12, 13]. Two photons entangled in OAM can also be generated in spontaneous four wave-mixing (SFWM) process in a hot atomic ensemble [14]. Fickler *et al.* [15] showed that using spiral phase mirrors, it is possible to transfer the state of polarization of a photon to a state with OAM encoding with OAM mode order l of 10010.

The OAM degree of freedom of light allows for fundamental studies of high dimensional (quantum) systems and quantum correlations. The fundamental studies of OAM include the demonstration of a spatially split coincidence pattern at the output of a parametric down converter pumped by a beam carrying OAM detected by directly using two point detectors [16]. Nagali *et al.* [17] observed a two-photon Hong-Ou-Mandel coalescence of photons carrying nonzero OAM. Leach *et al.* [18] demonstrated strong Einstein, Podolsky, and Rosen correlations between the angular position and the OAM of two photons created by SPDC. Mair *et al.* [13] provided a practical route to generate entanglement that involves many orthogonal OAM quantum states by using the SPDC source. Krenn *et al.* [19] created and verified the

two-photon entangled state of OAM in 100×100 high dimension. Bell inequality is used to demonstrate entanglement of two photons carrying OAM in high dimension [20–22]. These fundamental studies with photons carrying OAM show that the OAM is an useful degree of freedom for investigations of quantum communication and quantum information processing involving high-dimensional states.

OAM has other applications in quantum information science for informaiton processing and computation [23]. García-Escartín and Chamorro-Posada [24] theoretically proved a single photon encoded across several OAM modes can be manipulated with phase shifters, beamsplitters, holograms and OAM filters to implement any desired quantum computation. Another scheme implemented quantum walks with both OAM and spin angular momentum [25, 26]. Experiments realized Deutschs algorithm using linear optical components and CNOT gate with OAM modes [27–30].

The OAM degree of freedom of light can be used for information encoding for both classical and quantum communication. In classical communication, the OAM of light can be applied to increase the data transmission rate by multiplexing OAM together with frequency and polarization [31]. Data-transmission that is multiplexed by using OAM has allowed data transmition at the Terabit-scale, implemented in both free space [31] and fiber-based platforms [32]. In quantum communication, the OAM allows for encoding more than 1 bit of information per photon, which increases the channel capacity allowing for higher secret key rates and is used to tolerate noise and eavesdropping [33, 34]. High dimensional quantum key distribution (QKD) was implemented with OAM in free space [35–37]. Long-distance OAM transmission through free space in quantum communication process is of significant importance, since transmission of OAM in multimode fibers can't be implemented due to multimode mixing [38, 39]. However, it is challenging to transmit spatial modes over long distance since the transmission is distorted seriously by atmospheric turbulence. Paterson [40] characterized the decoherence effect of atmospheric turbulence on a communication system based on single-photon carrying OAM. Krenn *et al.* [41] investigated the transmission of OAM light modes and their superpositions over a 143-km free-space. Recently, the first experimental demonstration of QKD by

transmitting quantum states using photons prepared in four OAM modes in an air-core fiber has been demonstrated [42].

Beyond the applications in information processing and communication, light carrying OAM provides an ideal platform for investigations of protocols of state preparation and characterization of quantum states in high dimensions. A fundamental problem in quantum information science is the efficient and accurate determination of the state of a quantum system and the characterization of quantum processes via quantum tomography [43]. Quantum state tomography (QST) is the information processing task that allows for the reconstruction of an unknown state via measurement on multiple copies of the state [43]. Reconstruction of the quantum system requires making measurements to gather data that can provide sufficient information for accurate restoration. The most general kind of measurement is specified by a particular choice of positive-operator valued measure (POVM) [43]. The second step is the processing of the measurement outcomes, yielding a state that is most consistent with the data set given a particular estimation method, for example, maximum-likelihood estimation, together with constrains imposed by the physical system [44]. QST for high dimensional systems requires performing efficient, robust and accurate measurements in high dimensional spaces. Moreover, as the dimensionality of the system increases, the number of measurements required for QST substantially increases [45]. Different POVMs for QST can provide different ways for substantially reducing the number of measurements required for reconstructing the state by using prior information about the physical system, while still providing complete information about their quantum state [43]. For example, the symmetric informationally complete (SIC) POVM [46] and mutually unbiased bases (MUB) [47] are informational complete identifying uniquely a quantum state with the measurement statistics. However, the number of measurements for QST required by these two POVMs are substantially different [48]. This is because SIC POVMs use prior knowledge about the state, e.g., the state is close to pure, which allow them to reduce the number of meausrements for QST, a process that is called compress sensing [45]. Compressed sensing tomography is a powerful tool for investigating and characterizing high dimensional quantum states

that are close to pure, and quantum processes that are low rank. Techniques for compressed sensing can be applied to different processes for certain Hilbert dimension, and for different physical systems including photons [45] and atoms [43].

The goal of this thesis is to demonstrate a platform that can be used for the future investigations of different methods for QST for high dimensional quantum systems based on photons in Laguerre Gaussian (LG) modes in high dimensions, which is in principle, able to implement a diverse set of measurements that are used for the implementation of different POVMs [10]. By implementing different POVMs using the same platform, could allow for studies to compare the performance of various QST protocols and investigate their inherent efficiency, accuracy, and robustness to different sources of noise.

The work in this thesis is described as follows. In Chapter 2, we discuss the mathematical description of the Laguerre-Gaussian (LG) modes and the OAM content for beams in the paraxial approximation. This chapter also contains the description for the techniques used to generate and measure light in the LG basis, and the description of the experimental setup for this study. Chapter 3 describes the techniques that are used for correction of aberrations in the optical system, and the experimental implementation for state preparation of states of light with high OAM order. Chapter 4 describes our work in the investigation of projective measurements of states of light with OAM based on phase shaping techniques, and the characterization of efficiency and crosstalk achieved in the experimental setup. Chapter 5 contains the conclusions of this thesis.

Chapter 2

Generation and detection of light with OAM with SLMs

Light carries both spin angular momentum and OAM. The spin angular momentum is associated with circular polarization with amount of $\hbar$, and the OAM is caused by the azimuthal phase dependence $\exp(il\theta)$ of the phase front of the field, in which each photon in the beam carries an ammount of OAM equal to $l\hbar$. In this chapter, we describe the formulation of light beams in Laguerre-Gaussian modes and different methods for the generation and detection of light in the OAM basis. We describe the working principle of the spatial light modulator (SLM), which is a versatile tool for performing state preparation and detection of light carrying OAM with high fidelity and describe our the experimental setup for investigating the OAM mode generation and detection. We then discuss the theoretical efficiency limit for OAM detection based on the phase flattening technique using a SLM and a single mode fiber for performing projective measurements in the OAM basis [10].

2.1 OAM and Laguerre-Gaussian modes

Light carrying OAM has a helical phase, and results from the solution of the

paraxial Helmholtz equation in cylindrical coordinates. The solutions, containing information of the field distribution in cylindrical coordinates, are given by the Laguerre-gaussian modes. The light with helical phase $\exp(il\theta)$ can be decomposed with the complete set of Laguerre-Gaussian modes, which is the solution to paraxial Helmholtz equation in cylindrical coordinates. The Laguerre-Gaussian modes LG_l^p with radial and OAM quantum numbers p and l, respectively, are [49]:

$$\begin{aligned} \mathrm{LG}_l^p(\rho,\theta,z) &= \sqrt{\frac{2p!}{\pi(|l|+p)!}}\frac{1}{w(z)}\left[\frac{\sqrt{2}\rho}{w(z)}\right]^{|l|} L_p^{|l|}\left[\frac{2\rho^2}{w^2(z)}\right] \\ &\quad \times \exp\left[-\frac{\rho^2}{w^2(z)}\right]\exp\left[-\frac{ik\rho^2 z}{2(z^2+z_R^2)}\right] \\ &\quad \times \exp\left[i(2p+|l|+1)\tan^{-1}(\frac{z}{z_R})\right]e^{il\theta} \end{aligned} \tag{2.1}$$

where ρ is the radial coordinate, θ is the azimuthal angular coordinate and z is the coordinate that along the propagation direction of the beam. k is the wave vector. $w(z)$ is the spot size which is defined as the beam radius $w(z) = w(0)\sqrt{(z^2+z_R^2)/z_R^2}$ with minimum beam waist $w(0)$. z_R is the Rayleigh length defined as $z_R = \frac{kw(0)^2}{2}$ and $(2p+|l|+1)\tan^{-1}(\frac{z}{z_R})$ is the the Gouy phase [49]. $L_p^{|l|}$ are the associated Laguerre polynomials [49] with azimuthal index l, which is the number of intertwined helices, and radial index p, which is the number of radial nodes. Photons in an LG mode have well defined OAM which is equal to $l\hbar$, independently of their radial number.

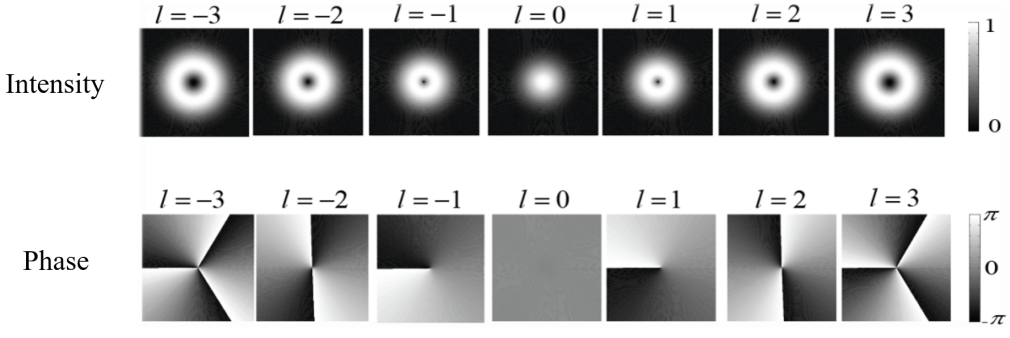

Figure 2.1: LG_l^0 intensity and phase patterns. OAM mode order l takes the value of $l = 0, \pm1, \pm2, \pm3$ and the intensity and phase patterns are observed at $z = 0$ transverse plane.

Figure 2.1 shows the intensity and phase patterns of LG modes with radial number

$p = 0$. For a beam carrying OAM, its helical wavefront has a wavevector that spirals around the beam propagation axis z. This means that the linear momentum of each photon has an azimuthal component in addition to the linear momentum along z direction [50]. The ratio between the azimuthal and the axial component of the linear momentum is $\frac{l}{k\rho}$. The linear momentum of one photon is $\hbar k$ along the z direction, thus the azimuthal component of momentum is $\frac{\hbar l}{\rho}$, which results in an orbital angular momentum per photon of $\hbar l$ [50].

There are several methods to generate light carrying OAM. One approach to generate light with helical phase front consists of sending a plane wave through an optical element with a helical surface, which is called the spiral phase plate [8]. The thickness of the spiral phase plate increases with azimuthal position according to $\frac{l\theta\lambda}{2\pi(n-1)}$, where n is the refractive index of the spiral phase plate and λ is the wavelength [8, 49]. Another method for generating light carrying OAM is based on the coupling between the OAM and spin angular momentum. The coupling between the OAM and the spin angular momentum can be achieved by a q-plate [9], which is a liquid crystal half-wave plate with a space-variant optical axis depending on azimuthal position. The order number q in a q-plate, which can be electrically tuned, denotes the rotating rate of the optical axis with respect to the azimuthal angle [51]. Light having zero OAM with left (right) circular polarization incidenting on a q-plate will be converted into light carrying OAM with $+2q\hbar, (-2q\hbar)$ per photon [52]. A third and widely used method to generate light carrying OAM is based on the holographic beam shaping techniques with reconfigurable holograms achieved with spatial light modulators (SLMs). This technique is very versatile, and allows for inducing arbitrary phase shifts from 0 to 2π of an incoming beam. Efficient and high fidelity generation of light beams with helical phase can be achieved by preparing a diffracting fork grating with the SLM when the SLM is illuminated by a plane wave and the desired beam is prepared in the first diffraction order. Moreover, phase-only SLMs can be used to modulate both phase and amplitude of an incident beam by using diffracting holograms with modulated diffraction depths. In our experiment, investigation of state preparation and measurement of light with OAM is achieved by

using phase-only SLMs, which is a powerful technique for preparation of light with programmable field distributions, as discussed with more details in the next sections.

In analogy to state preparation of light with OAM, there are several techniques for measurement of light with structured phase fronts. Different interferometric methods can allow for distinguishing light in arbitrarily many OAM states. The interferometric techniques based on mode converters can use a combination of cylindrical lenses to induce a shift of the Gouy phase between the modes [53], or a dove prism that can invert any image into its mirror image [54]. These induced phase shifts allow for the OAM of a laser beam containing many photons in the same mode to be measured via interfering a beam with its mirror image [55, 56]. In Ref. [57], Leach *et al.* distinguished photons in arbitrary OAM states with a Mach-Zehnder interferometer and a dove prism, which is capable of separating even and odd OAM modes. Cascading additional Mach-Zehnder interferometers in principle enables to distinguish individual photons in arbitrary OAM states with high mode order l. Recent advances in interferometric techniques have been shown useful for sorting not only OAM modes with different l orders but also modes with different radial orders at the single photon level [58]. Even though these techniques are very powerful for mode sorting and are expected to become more robust and scalable, these techniques are not easy to implement, and require a careful alignment and high stability. In our work, we instead investigate a much simpler technique for measurement of OAM modes that allows for performing projective measurements onto arbitrary spatial modes. We detect the OAM modes by using a SLM to project the LG modes into the fundamental Gaussian LG_0^0 mode and coupling it into a single mode fiber (SMF) which effectively works as a spatial mode filter. This technique is called phase flattening [10]. The details of the implementation are described in Section 2.4.

2.2 Spatial Light Modulator

The LCOS spatial light modulator (SLM) is a device that can be used to alter

the polarization or the phase of an incident light beam utilizing the electrically-modulated optical properties of liquid crystals (LCs). The LCOS SLM technology combines the unique light-modulating properties of liquid crystal (LC) materials and the high-performance silicon complementary metal oxide semiconductor (CMOS) technology through dedicated LCOS assembly process [59]. A LCOS device can be either transmissive or reflective. Currently, there are two types of LCOS SLMs, amplitude modulation SLM and phase modulation SLM. For amplitude modulation, the amplitude of the light is changed by varying the linear polarization direction of the incident light passing through a linear polarizer. For phase-only modulation, the phase delay is accomplished by electrically adjusting the optical refractive index along the light path, which is possible because of the non-zero birefringence of the LC materials. High light reflection efficiency can be achieved by using the phase modulation process since no light is absorbed by the polarizers or other light absorbing components. Moreover, it is possible to achieve both phase and intensity modulations using phase-only SLMs, which then allows for preparation of light modes with arbitrary phase and intensity profiles.

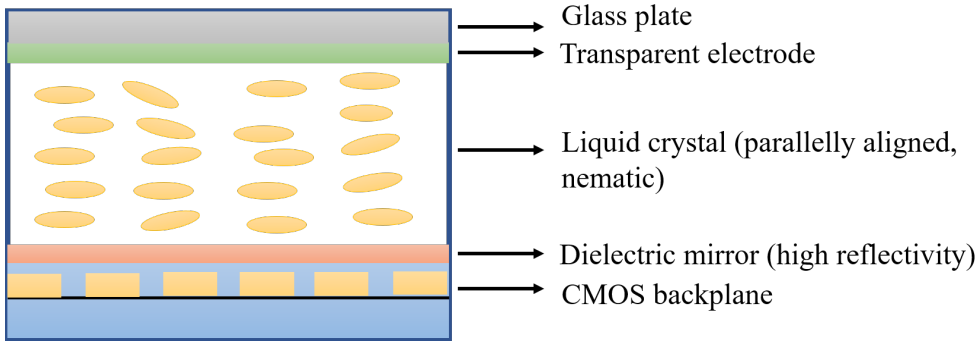

Figure 2.2: Structure of the SLM. The liquid crystal molecules are parallelly aligned to the CMOS backplane and front surface. When voltage is applied to the backplane, the arrangement of the liquid crystal molecules can be changed. This produces a change in the refractive index and modulate the phase of the incoming beam.

The basic structure of the LCOS SLM is a parallel aligned LC layer sandwiched between a cover glass and a CMOS backplane. Figure 2.2 shows the structure of a reflective SLM. The silicon CMOS backplane consists of the electronic circuit that

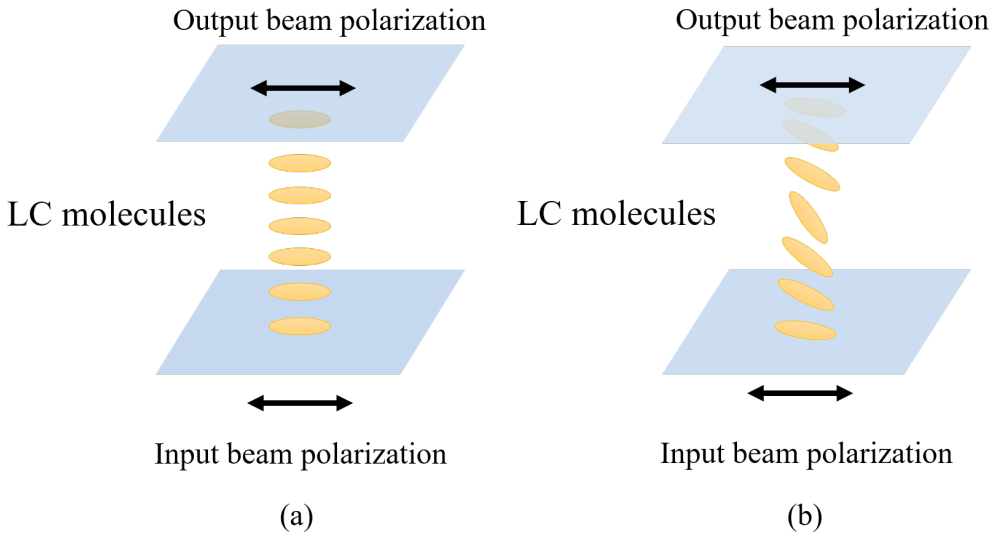

Figure 2.3: The liquid crystal molecule alignment (a): The liquid crystal molecules are parallelly aligned to the backplane in the same direction when zero voltage applied to the CMOS back plane. (b): The molecules tilt and change the refractive index.

is buried under pixel arrays to change the voltage for each pixel, allowing for local control of the induced electric field. By applying the voltage to the pixelated electrode on the CMOS backplane, the orientation of the liquid crystal molecules changes in the LC layer and thus changes the refractive index. When the SLM is off, all the LC molecules are parallelly aligned to the backplane in the same direction, as shown in Fig. 2.3 (a). When the SLM is on, the molecules tilt as shown in Fig. 2.3 (b), thus the phase retardation has been changed [60]. This procedure allows the SLM to achieve controllable phase modulation and preserves the direction of polarization of light when the polarization direction of the incident light is parallel to the direction of the LC molecules. The dielectric mirror (see Fig. 2.2) enables the device to have high reflectivity about $80 \sim 95\%$, depending on the mirror design for optimized performance for a given wavelength and bandwidth.

In our experimental investigations, we use a LCOS-SLM device from Hamamatsu LCOS SLM X10468-01. This device is a reflective type phase-only spatial light modulator, and its phase modulation can be accomplished by sending a computer-generated hologram to the SLM via a digital-video-interface (DVI) signal. The SLM

in our experiment has 600×792 pixels, each pixel with square area $20\mu\text{m} \times 20\mu\text{m}$. The response time measured of the SLM is about 30ms with a maximum refresh rate of $60Hz$. The SLM has a bitdepth of 8 bits, which means it has 256 signal levels setting the resolution for phase modulation. The phase induced by the SLM on a light beam changes linearly with the input signal voltage. This linear relation allows to easily map changes in voltage to changes in phase. LCOS-SLM is designed to have phase modulation of more than 2π radians over $400 - 1500$nm wavelength, and we use a laser source of light at 850nm keeping the phase modulation within a range of $[0, 2\pi)$ [61].

This phase-only LCOS SLM shows high reflectivity, high light utilization efficiency, and good linear phase dependence with voltage change and can be easily controlled by computer. These advantages make phase-only LCOS SLMs very useful for diverse applications, including real-time holography, optical correlators [62], wavelength selective switches, reconfigurable optical add-drop multiplexers [31], and using them as diffractive optical components [59]. We use phase-only SLMs for state preparation and state projection of OAM states, and investigate different methods using SLMs for aberration correction due to experimental imperfections with the goal of achieving high fidelity on the preparation and measurement of OAM states in high l orders. Below we describe the principles for the generation and detection of OAM modes using phase-only SLMs, including the description of the optical transformation by lenses required for preparing and filtering modes in the spatial structure, and for performing projective measurements onto arbitrary OAM states.

2.3 Optical Fourier transform

State preparation and detection of OAM modes using beam shaping techniques based on SLMs with high efficiency and fidelity, require specific optical arrangements for filtering and performing optical Fourier transforms in the spatial domain based on lenses and free-space propagation, as described below.

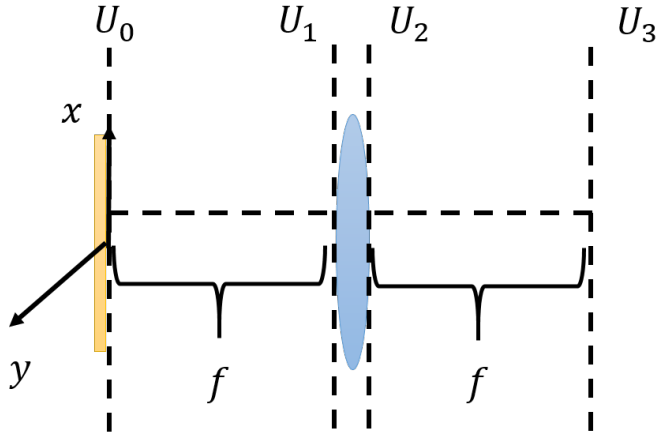

Figure 2.4: A light field incident on a lens at a distance equal to the focal length f with field $U_0(x_0, y_0)$ and the light field at the focal plane of the lens becomes $U_3(x_3, y_3)$.

Consider a beam with electric field $U_0(x_0, y_0)$ incidents on a lens at a distance equal to the focal length of the lens f, as shown in Fig. 2.4. Denoting the field at the front surface of the lens as $U_1(x_1, y_1)$, the field right after the lens as $U_2(x_1, y_1)$ and the field at the focal plane as $U_3(x_3, y_3)$, it is possible to describe the relationship between these fields by using difraction theory. $(x_0, y_0), (x_1, y_1), (x_3, y_3)$ represent the coordinates on the transverse plane. By applying the Fresnel diffraction equation, as described in the Appendix A, Eq. (A.16), we obtain:

$$U_1(x_1, y_1) = \frac{-e^{-ikf}}{i\lambda f} e^{\frac{-ik}{2f}[x_1^2+y_1^2]} \iint_{-\infty}^{+\infty} U_0(x_0, y_0) e^{\frac{-ik}{2f}[x_0^2+y_0^2]} e^{i\frac{2\pi}{\lambda f}[x_0x_1+y_0y_1]} dx_0 dy_0 \quad (2.2)$$

which describes the electric field at an arbitrary point (x_1, y_1) before the lens, expressed as the integral of the electric field $U_0(x_0, y_0)$ over the whole transverse plane (x_0, y_0), assuming x_0 and y_0 are much smaller than f.

When the beam passes through a thin lens, it undergoes a phase transformation, and the phase transformation function can be expressed as $t(x_1, y_1) = e^{-ikn\Delta_0} e^{i\frac{k}{2f}(x_1^2+y_1^2)}$ (See Appendix A, Eq. (A.29)), where Δ_0 is the lens thickness in the optic axis and n is the refractive index. The field $U_2(x_1, y_1)$ after the lens can be described as:

$$U_2(x_1, y_1) = U_1(x_1, y_1) t(x_1, y_1) \quad (2.3)$$

$$= \frac{-e^{-ikf}}{i\lambda f} e^{-ikn\Delta_0} \iint_{-\infty}^{+\infty} U_0(x_0, y_0) e^{\frac{-ik}{2f}[x_0^2+y_0^2]} e^{i\frac{2\pi}{\lambda f}[x_0x_1+y_0y_1]} dx_0 dy_0$$

Applying the Fresnel diffraction equation again, we obtain $U_3(x_3, y_3)$:

$$\begin{aligned} U_3(x_3, y_3) &= \frac{-e^{-i2kf}}{\lambda^2 f^2} e^{-ikn\Delta_0} e^{\frac{-ik}{2f}(x_3^2+y_3^2)} \\ &\iiiint_{-\infty}^{+\infty} U_0(x_0, y_0) e^{\frac{-ik}{2f}[x_0^2+y_0^2]} e^{i\frac{2\pi}{\lambda f}[x_0x_1+y_0y_1]} \\ &e^{\frac{-ik}{2f}[x_1^2+y_1^2]} e^{i\frac{2\pi}{\lambda f}[x_1x_3+y_1y_3]} dx_0 dy_0 dx_1 dy_1 \end{aligned} \tag{2.4}$$

Consequently,

$$\begin{aligned} U_3(x_3, y_3) &= \frac{-e^{-i2kf}}{i\lambda f} e^{-ikn\Delta_0} \\ &\iint_{-\infty}^{+\infty} U_0(x_0, y_0) e^{-i\frac{\pi}{f\lambda}(x_0^2+y_0^2)} e^{i\frac{2\pi}{f\lambda}(x_3x_0+y_3y_0)} dx_0 dy_0 \end{aligned} \tag{2.5}$$

By making a far field approximation (assume x_0 and y_0 are much smaller than f) and ignore the constant phase factor,

$$U_3(x_3, y_3) = \frac{1}{\lambda f} \iint_{-\infty}^{+\infty} U_0(x_0, y_0) e^{i\frac{2\pi}{f\lambda}(x_3x_0+y_3y_0)} dx_0 dy_0 \tag{2.6}$$

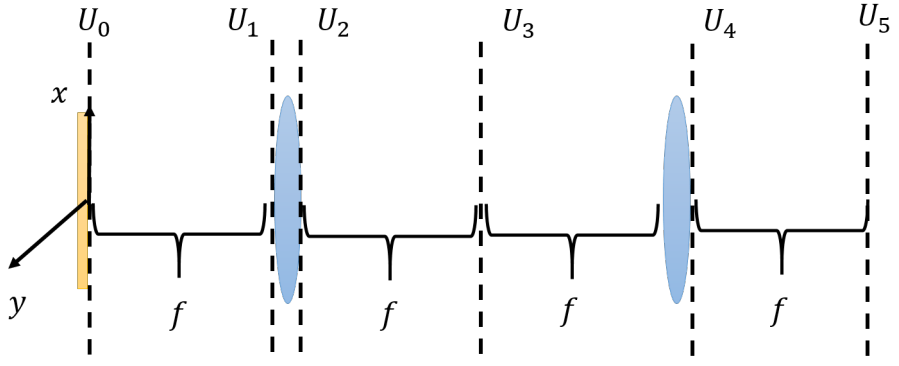

Figure 2.5: The $4f$ system is a commonly used optical relay that consists of two positive lenses with the input plane located on the focal length f in front of the first lens with input field $U_0(x_0, y_0)$ and the output plane located on the focal length f after the second lens with output field $U_5(x_5, y_5)$.

This calculation shows that the lens performs a Fourier transform for the initial field U_0 with a scale factor. An additional operation/manipulation required in the optical setup in the experiment for OAM state preparation and detection is spatial filtering and imaging based on a 4f-system. This filter allows for selecting the first-order diffraction from the blazed grating induced in the SLM for preparation of OAM modes, and image the state prepared in one SLM onto a second SLM. This procedure will be described in the next section. A 4f-system is composed by a two-lens arrangement with focal length f, separated as shown in Fig. 2.5. Considering the initial field $U_0(x_0, y_0)$ and the field $U_5(x_5, y_5)$ at the focal plane of the second lens, we can investigate the transformation of $U_0(x_0, y_0)$ by 4f-system by applying Eq. (2.6) twice to obtain $U_5(x_5, y_5)$:

$$\begin{aligned} U_5(x_5, y_5) &= \frac{1}{\lambda^2 f^2} \iiint_{-\infty}^{+\infty} U_0(x_0, y_0) e^{i\frac{2\pi}{f\lambda}(x_3 x_0 + y_3 y_0)} e^{i\frac{2\pi}{f\lambda}(x_5 x_3 + y_5 y_3)} dx_0 dy_0 dx_3 dy_3 \\ &= 4\pi^2 \frac{1}{\lambda^2 f^2} \iint_{-\infty}^{+\infty} U_0(x_0, y_0) \delta(\frac{2\pi}{\lambda f}(x_5 + x_0)) \delta(\frac{2\pi}{\lambda f}(y_5 + y_0)) dx_0 dy_0 \\ &= U_0(-x_5, -y_5) \end{aligned} \tag{2.7}$$

We observe that the 4f-system image the initial field on the focal plane of the second lens. We use the 4f-system to image SLM1, which is used to prepare the input state, onto a second SLM (SLM2), which is used to perform mode transformations for projective measurements onto the OAM space. Thus we can perform the projective measurement. This will be shown in the next section.

2.4 OAM mode generation and detection

SLMs provide an easy and versatile way to generate and manipulate optical fields from using computer generated holograms. Phase-only SLMs allow for manipulating the phase of the light beams with an arbitrary phase profile $\Psi(x_0, y_0)$, in the $0 - 2\pi$ range, where x_0, y_0 are the transverse coordinates on the SLM plane. For an input plane wave, the phase transformation induced by a SLM converts the plane wave

into $T(x_0, y_0) = \exp(i\Psi(x_0, y_0))$ when reflected by the hologram. A direct way of generating OAM modes using phase-only SLMs is to encode a diffraction phase grating and a helical phase profile $l\theta$ in the SLM. The diffraction grating diffracts the input beam into different diffraction orders on the far field. We select a particular diffraction order, commonly the first order, which allows for preparation of arbitrary modes, such as LG modes, as shown in Fig. 2.6. Using a lens to perform an optical Fourier transform on the focal plane of the lens, allows to achieve a similar transformation as what would be achieved in the far field (see Section 2.3 and Appendix A). After we generate the LG mode with SLM1, it is possible to use a lens to detect the intensity pattern of LG mode by a CCD at the focal plane of a Fourier lens (F3), and using an iris to select the first order diffracted mode. The experimental setup for the preparation of OAM states with a SLM and the observation of the far field intensity distribution are shown in Fig. 2.7. Thus an input Gaussian light beam can be converted into a helical mode whose wave front resembles a l fold corkscrew [49] at the focal plane of lens F3, and the intensity pattern can be detected on the CCD.

Phase-only SLMs allow for simultaneously modulating both phase and amplitude of an optical field by using diffraction techniques, as described below for the preparation of optical fields with arbitrary phase and intensity distributions. In general, it is possible to control the intensity of the diffracted modes by modulating the grating depth in the SLM. To understand how to encode intensity and phase with a phase-only SLM, we can consider first the effect of the diffraction grating, and then the modulation of this grating.

A blazed grating has a phase profile $\Psi(x_0, y_0) = mod(2\pi x_0 MD, 2\pi)$, where $1/D$ is the spatial period and M defines the extent of the phase shift over each period of the grating, which varies in the range $0 \leq M \leq 1$. The phase in the grating increases linearly from a minimum value of zero to a maximum value of $2\pi M$. Considering an incident plane wave, then the output wave after diffraction by this grating becomes $T(x_0, y_0) = \exp[i \cdot mod(2\pi x_0 MD, 2\pi)]$ and can be expanded in a Fourier series as [63]:

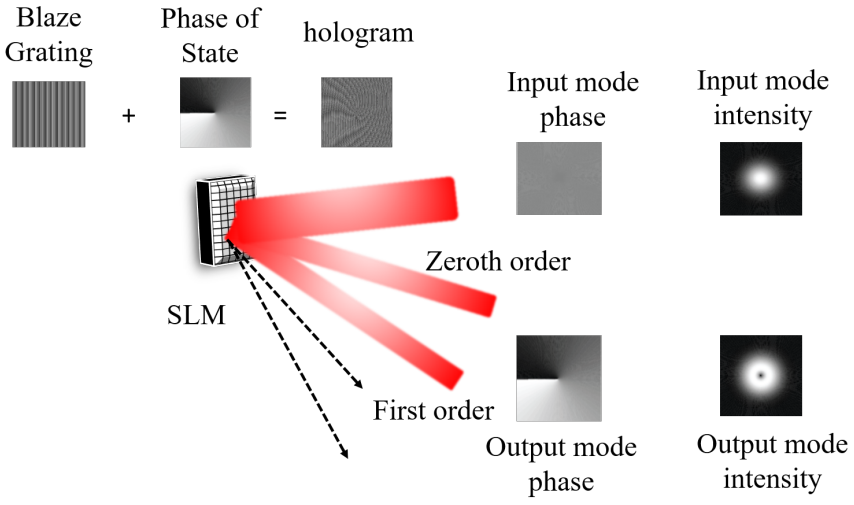

Figure 2.6: A beam incident on a SLM with a hologram containing a phase grating and the phase profile $l\theta$ with $l = 1$. The light diffracted on the first order mode is the desired field of LG_1^0.

$$T(x_0, y_0) = \sum_{-\infty}^{+\infty} T_n \exp(i2\pi n D x_0) \tag{2.8}$$

where the coefficients T_n are given by:

$$T_n = \exp[i(n - M)\pi] \frac{\sin[\pi(n - M)]}{\pi(n - M)} \tag{2.9}$$

After taking the Fourier transform [63], the field in the Fourier plane is:

$$t(x_3, y_3) = \sum_{-\infty}^{+\infty} T_n \delta(x_3 - nD) \tag{2.10}$$

where x_3, y_3 are coordinates on the Fourier plane, which is the focal plane of lens F3. Therefore the diffraction pattern consists a series of delta functions whose amplitudes are given by the coefficients T_n, and the total energy is distributed between different diffraction orders n. For $M = 1$, all the light is, in theory, diffracted into the first order $n = 1$, since $T_1 \leq 1$. As M decreases, the intensity of the light diffracted into the first order decreases when the light energy in the zeroth order increases. Then, by using a spatially varying function $M(x_0, y_0)$, it is possible to modulate the amplitude of the diffracted modes in the first order. Therefore, this possibility

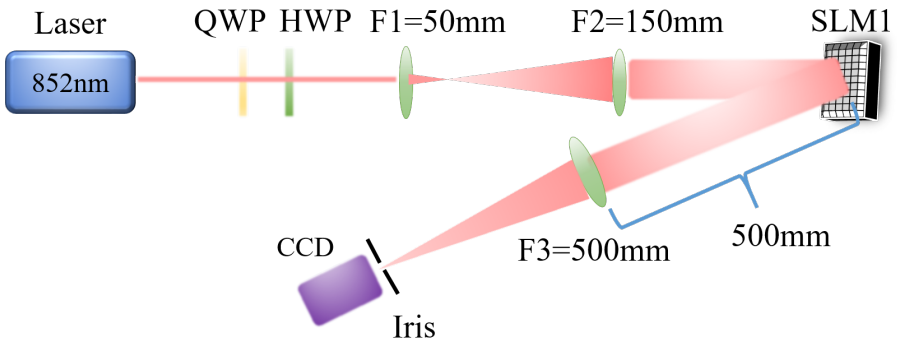

Figure 2.7: Experiment setup for the generation of LG modes. A quarter (QWP) and a half (HWP) waveplates are used to ensure linear polarization for the incident field, and lenses F1 and F2 expand the beam by ×3. After diffraction by the spatial light modulaator (SLM1), the lens F3 allows to perform a Fourier transform for the light diffracted by SLM1 on its focal plane. The iris filters out other order modes except for the first order diffracted mode by the grating encoded in the SLM1. The LG modes intensity generated by SLM1 can be detected by the CCD after the iris.

allows for encoding both the desired phase and amplitude by using a phase-only SLM. The amplitude can be encoded on to the hologram, such that the desired pattern is diffracted into the first order, while the unwanted light remains in the zeroth order. An exact solution for encoding both the phase and amplitude profile with a phase only SLM for any given paraxial mode in the focal plane of F3, is described in Ref. [64]. Consider a desired output beam at the focal plane of F3:

$$E(x_3, y_3) = A(x_3, y_3)e^{(i\Phi(x_3,y_3))} \tag{2.11}$$

It is in principle possible to generate this target field by a phase-only SLM from a given input field. For an incident plane wave, the field after diffraction by the SLM can be expressed as:

$$T(x_3, y_3) = \exp[iM(x_3, y_3)mod(H(x_3, y_3) + 2\pi x_0 D, 2\pi)] \tag{2.12}$$

where $M(x_3, y_3)$ is a normalized bounded positive function of amplitude of the target field in Eq. (2.11) with $0 \leq M(x_3, y_3) \leq 1$, which modulates the depth of the diffraction grating. $H(x_3, y_3)$ is an analytical function of the amplitude and phase profiles of the desired field in Eq. (2.11). Then, the first order diffraction has a

Fourier coefficient given by [64]:

$$T_1(x_3, y_3) = -\text{sinc}(\pi M - \pi)e^{i(H+\pi M)} \tag{2.13}$$

with

$$\begin{aligned} M &= 1 + \frac{1}{\pi}\text{sinc}^{-1}(A) \\ H &= \Phi - \pi M \end{aligned} \tag{2.14}$$

where $\text{sinc}(x) = \frac{\sin(x)}{x}$ is sinc function and sinc^{-1} stands for the inverse sinc function. This is an exact way of encoding the amplitude and the phase of an optical field into a phase-only hologram and can be used to control both the phase and amplitude of the incident light. Using this technique, it is possible to prepare modes with arbitrary phase and intensity. Figure 2.7 shows the experimental setup to investigate the state preparation using a CCD camera. Figure 2.8 shows the intensity pattern for the generation of LG mode LG_5^0 and superpositions including the theoretical predictions.

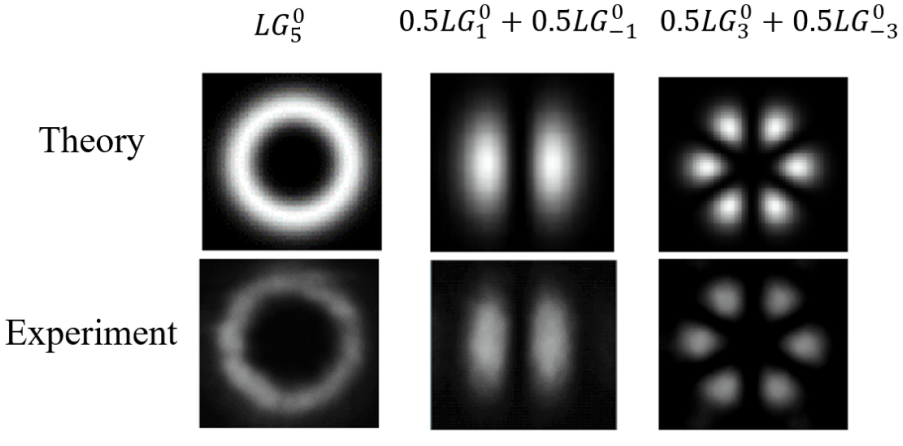

Figure 2.8: LG modes generated at the focal plane of lens F3. The figure displays the generated mode intensity pattern of LG_5^0, $0.5 \cdot \text{LG}_1^0 + 0.5 \cdot \text{LG}_{-1}^0$ and $0.5 \cdot \text{LG}_3^0 + 0.5 \cdot \text{LG}_{-3}^0$, comparing with the theoretical intensity pattern of those modes.

The transformations enabled by phase-only SLMs allow also for performing projective measurements onto different spatial modes, such as LG modes and superpositions. These projective measurements can be achieved by using a second SLM to perform a

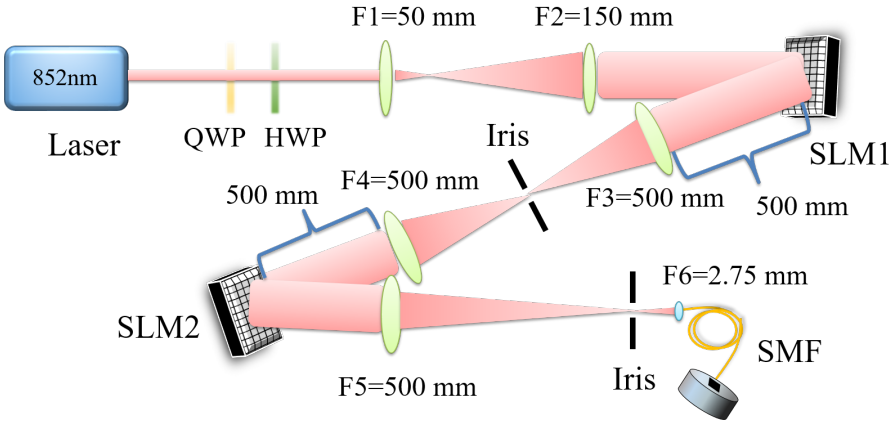

Figure 2.9: Experimental setup. SLM1 is imaged on SLM2 by a 4f-system with an iris on the focal plane of lens F3. By encoding SLM2 with a conjugate mode of the mode generated by SLM1, the mode generated can be project into a LG_0^0 mode, which overlaps with the fundamental mode of the fiber and can be coupled into the single mode fiber.

mode transformation and a single mode fiber (SMF) used as a spatial filter to select only one spatial mode, in which the projection is being performed. Consider that the mode generated by a first SLM (SLM1) is $\mathrm{LG}_l^p(\rho,\theta,z)$, then a second SLM (SLM2) can be encoded to perform a mode transformation corresponding to the conjugate mode $[\mathrm{LG}_{l'}^{p'}(\rho,\theta,z)]^*$. After diffraction by the second SLM (SLM2), the light field becomes $[\mathrm{LG}_l^p(\rho,\theta,z)[\mathrm{LG}_{l'}^{p'}(\rho,\theta,z)]^*]$. Therefore, the far field distribution by taking a 2D-Fourier transform [1] is:

$$\mathcal{F}_{p,l}(r,\phi) = \mathcal{FT}[\mathrm{LG}_l^p(\rho,\theta,z)[\mathrm{LG}_{l'}^{p'}(\rho,\theta,z)]^*] \tag{2.15}$$

in which $\mathcal{FT}$ represents the 2D Fourier transform and r,ϕ are the cylindrical coordinates in the far field. This transformation can be performed by a second lens. Considering the case $p = p' = 0$ and only when $l = l'$, the transformed mode in the far field is close to the fundamental Gaussian mode, and this mode shows a high overlap with the fundamental mode of a SMF, which only transmits its fundamental mode. As a result, when SLM2 encodes the conjugate mode that is generated by SLM1 (LG_l^0), thus Eq. (2.15) becomes (with $p = p' = 0$):

$$\mathcal{F}_{p,l}(r,\phi) = \frac{2\pi e^{\frac{i\pi}{\lambda f}r^2}}{i\lambda f}\int_0^\infty \rho d\rho |\mathrm{LG}_l^0|^2 J_0(\frac{2\pi}{\lambda f}r\rho) \tag{2.16}$$

where J_0 is the zero order Hankel transform. The intensity distribution of the projection in the far field shows in Fig. 2.10. The mode projection results in a bright center spot with a ring outside it. The radius of the spot changes with the mode order l. Figure 2.11 shows the experimental result for the preparation of projection of state LG_3^0. Note that after the projection operation, the intensity at the focal plane of the fourier lens after the SLM2 approximates a Gaussian intensity distribution. Since the Gaussian modal distribution has a high overlap with the fundamental mode of the SMF, we can place a SMF in the far field as a Gaussian mode filter to implement the projective measurement. The coupling efficiency of the spatial mode after projection to a SMF is obtained by integrating the far field modal distribution over the Gaussian mode of the SMF [1]:

$$\eta_p^l = \frac{2}{\pi\sigma^2}\left| \int_0^\infty r dr \int_0^{2\pi} d\phi \mathcal{F}_{p,l}(r,\phi) e^{-\frac{r^2}{\sigma^2}} \right|^2 \tag{2.17}$$

where σ is the beam waist radius of the SMF. For $p = 0$,

$$\eta_0^l = \frac{|l|!^2}{(2|l|)!} C^{2|l|+1} G \tag{2.18}$$

where $C = 2/(1+\frac{\sigma^2}{a_0^2})$, $G = 2/(1+\frac{a_0^2}{\sigma^2})$ and $a_0 = \frac{\sqrt{2}\lambda f}{\pi w(0)}$ is the natural scaling factor at the fiber. Figure 2.12 shows the theoretical coupling efficiency of projective measurements for the LG_l^0 modes changing with $l = 0, 1, \cdots, 5$.

In our experiment, the LG mode is generated by SLM1 and projected onto the second SLM (SLM2) via a 4f-system mentioned in Section 2.3. The first-order diffracted mode is selected by the iris placed at the focal plane of lens F3. SLM2 converts the LG modes generated by SLM1 to the LG_0^0 in the far field and then this mode is coupled into a single mode fiber (SMF). Figure 2.11 shows the projective measurement result for a prepared state LG_3^0 and the images after projection in the far field by replacing the SMF with a CCD after the iris.

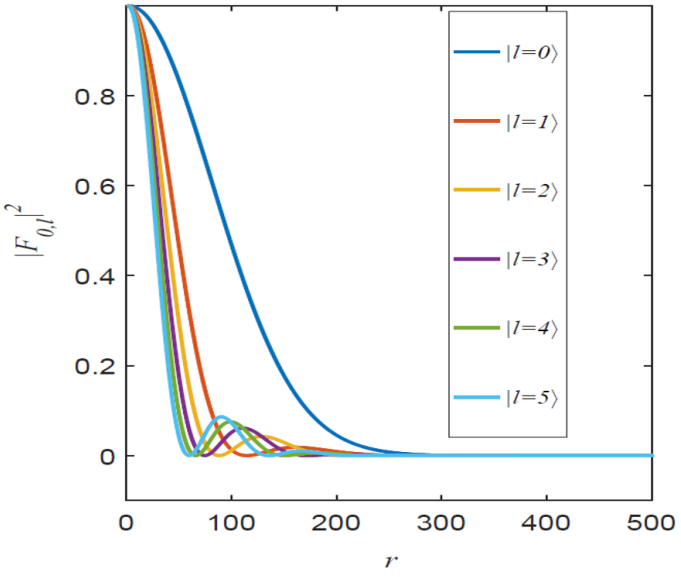

Figure 2.10: Intensity of LG_l^0 at the input to the fiber with $l = 0, 1, \cdots, 5$ as a function of the radius distance r. The plots are generated based on the equations in Ref. [1].

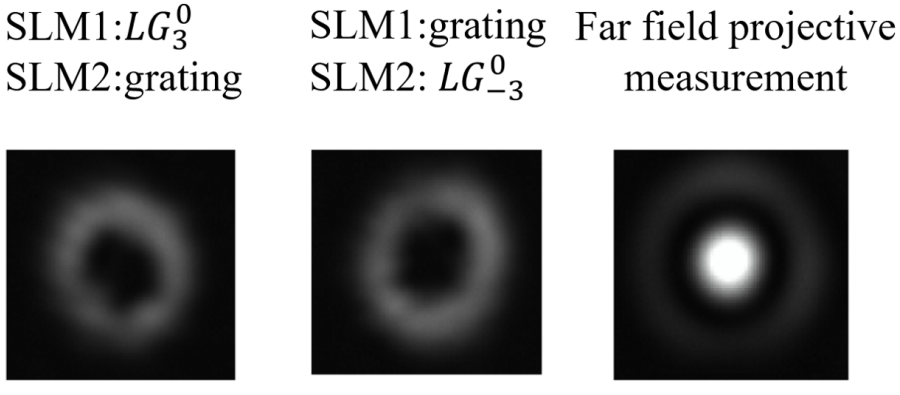

Figure 2.11: Intensity pattern of LG_3^0 projection on the far field taken by the CCD. The SLM1 generates a LG_3^0 mode and the SLM2 encodes a conjugate LG_{-3}^0 mode. The projection in the far field shows a Gaussian spot in the center with rings outside.

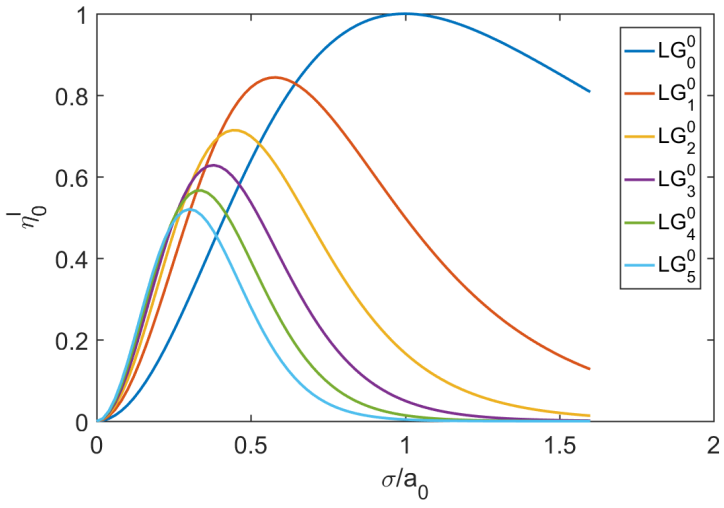

Figure 2.12: Coupling efficiency for projective measurements for the LG_l^0 mode changing with $l = 0, 1, \cdots 5$. The plots are generated by using equations described in Ref. [1]

2.5 Conclusions

In this chapter, we reviewed the description of light beams with helical phase front, which have a well defined orbital angular momentum (OAM). The Laguerre-Gaussian modes which are the solutions to paraxial Helmholtz equation in cylindrical coordinates, form a complete basis of the spatial distribution of light carrying OAM. We described our experimental setup that can be used to generate and detect light beams in arbitrary LG modes, as shown in Fig. 3.8. We use phase-only LCOS SLMs to control both the intensity and the phase of the beams profile by imprinting a computer generated hologram on SLM, which allows to generate the LG modes and their superpositions and perform projective measurements in the LG basis. The projective measurements of the prepared mode are performed by encoding on the second SLM the phase of the conjugate mode which we want to project onto. This operation generates a Gaussian-like mode in the far field. Coupling this mode into the SMF allows to perform the projective measurement of specific LG mode. The coupling efficiency into the SMF of the mode resulting from the projection is mode

dependent and shows a bias towards higher mode order l.

Chapter 3

Wavefront distortion correction based on SLMs

The generation of spatial modes carrying OAM using beam shaping techniques is very susceptible to imperfections and misalignments of realistic optical setups, and result in distorted modes. This is due to the aberrations caused by all optical components in the mode generation process. In this chapter, we provide an overview of the main optical aberrations that cause mode distortion in our setup in Section 3.1. Then we discuss different optical aberration correction methods that can be implemented with beam-shaping techniques based on SLMs. We introduce the method we use to correct the aberrations in our experiment and describe our experimental results for mode generation and mode projection operations after aberration correction using SLMs.

3.1 Wavefront aberration

The departure from idealized conditions of Gaussian optics are known as aberrations. In an ideal optical imaging system, all rays of light from a point in the object plane would converge to the same point in the image plane, forming a clear

image. The effects which cause different rays to converge to different points are called aberrations [65]. More specifically, it can be defined as the departure from paraxial optics of an optical system [66]. There are two main types of aberrations: chromatic aberrations (which arise from the fact that refraction index depends on the frequency of the light) and monochromatic aberrations. For monochromatic light, only monochromatic aberrations need to be considered. An aberration-free imaging system can be treated as a combination of linear optical components, so the image can be traced back to each point on the object via those rays. This image is called an aberration free image, the quality of the image is only diffraction-limited.

Aberrations ignored by the paraxial approximation which is used to derive the first-order theory of the geometric optics are crucial. The paraxial treatment of light propagation in optical systems is based on the assumption that a light should be incident in an optical element with a small angle and very close to the optical axis, namely $\sin\varphi \approx \varphi$, where φ is the angle between the ray and the optical axis. However, to consider more realistic situations, the third order theory of light propagation should be taken into account including the first two terms in the following expansion as an improvement of the paraxial approximation [67]:

$$\sin\varphi = \varphi - \frac{\varphi^3}{3!} + \frac{\varphi^5}{5!} - \frac{\varphi^7}{7!} + \cdots \tag{3.1}$$

Departure from the first order theory are embodied in the five primary aberrations: spherical aberration, coma, astigmatism, field curvature and distortion [65]. These are the aberrations that influence our mode generation quality.

3.2 Methods for wavefront correction

Encoding information in the transverse field profile of light using orthogonal modes, such as Laguerre-Gaussian modes, can allow for increasing the amount of information that can be carried by single photons for communication and information processing. However, any aberration experienced by light caused by optical wavefront

manipulations and propagation through optical components will severely limit the ability to decode this information. Therefore, to achieve transmission of information with high fidelity, it is necessary to have efficient and reliable techniques for aberration correction. SLMs are important tools for beam shaping and can be in principle used for preparation of light in different transverse spatial modes and for correction of aberrations. The reflective SLM, which has a shorter reaction time compare to transmissive SLM, has a non flat (uneven) reflective surface and usually lead to unwanted, mostly astigmatic distortions in the phasefront of the incident light beams. In a typical experiment where SLMs are used for state preparation, the beam is subject to wavefront distortion due to the non-Gaussian profile of the incoming beam, the non ideal behavior of all the optical components before the final target plane (the plane where we detect the generated modes) and the surface curvature of the SLMs. These aberrations decrease the performance of beam shaping for state preparation, especially for the Laguerre-Gaussian (LG) modes, which are very sensitive to such distortions [68]. Even small phase irregularities would cause significant deformation of the circular shaped OAM modes on the image plane of the fourier lens in the optical systems for detecting such modes (see Chapter 2). This makes the process of generating LG modes and performing projective measurements with SLMs challenging, particularly for LG modes living in a high dimensional Hilbert space for applications in quantum information protocols.

State preparation of OAM modes using SLMs requires calibration of the surface flatness of the SLM, since any deviation from a flat surface causes unwanted phase distortion in the transverse modes. Different methods have been proposed to calibrate the flatness of the SLMs surface and correct for phase distortion. In the early work [69, 70], interferometric methods used for surface metrology were applied to measure small wavefront deformations caused by SLMs. In [69], Dou, *et al.*, used a Mach-Zehnder interferometer to obtain the interference from a transmissive SLM with a reference beam. This interference pattern represents the relative phase front variation of the two paths, and the fringe distortion on the pattern provide information about the surface curvature of the SLM. In these experiments, aberration correction was

performed using closed loop adaptive method with the SLM to operate as a wavefront corrector. Adaptive wavefront control can also be performed in other interferometric systems such as, based on Twyman-Green[70], Fizeau, Zygo inteferometers [71]. These methods achieve reduction of phase aberration and reach the diffraction-limited wavefront correction of static aberrations by using SLM for precise wavefront control.

As an alternative to interferometry method, a quite powerful method uses the Shack-Hartmann wavefront sensor to calibrate the distorted wavefront, which is not only simple and compact, but also relatively insensitive to vibration [72, 73]. In this technique, the SLM screen is divided into small circular apertures, each of the aperture is encoded with a different blazed diffraction grating. The displacement of each spot on the image plane of a Fourier lens is proportional to the wavefront distortion which can be used to recover a phase map of the aberration [72]. However, while this method is relatively simple to implement, the size of each spot increases when decreases the pitch grating size on the SLM. This places an upper bound on the spatial frequencies which can be detected and corrected for.

Another widely used method for phase distortion correction is phase retrieval, which utilizes the iterative Gerchberg-Saxton (GS) algorithm to reconstruct the phase map. The algorithm can be implemented by a SLM encoded with a LG_1^0 phase only hologram with a finite circular aperture [68]. The initial hologram provides the ideal field distribution on the image plane of a lens. The theoretical amplitude on the image plane is compared with the amplitude of the real image. The aberration phase map is extracted by subtracting the initial LG_1^0 phase hologram. This method not only corrects the phase error caused by the SLM, but also the phase errors introduced by the other optical components in the optical pathway. However, the method is highly sensitive to the initial conditions. It assumes that the correct phase hologram lies close enough to the original phase hologram. The phase retrieval is not unique and the algorithm converges to the local minimum.

Another method for aberration detection and correction based on interference, uses the idea of directly interfering two or more active regions on the SLM to obtain information about the phase distortion that can be used for error correction. This

technique, described in Ref. [74], Čižmár, Tomáš *et al.* use two small patches on the SLM in which they encode a blazed grating to diffract the incoming beam and optimize the intensity value on the Fourier plane. As an extension of this method, it is possible to use multibeam interference on the focal plane of the Fourier lens in which beams are diffracted by different small pieces of grating on the SLM [75]. The method that we use in our experiment follows [76], which is also a method of using the diffracted beam interference from two part of the SLM to construct the phase map for wavefront correction. In general, the aberration correction method we use can correct for optical aberrations caused by all optical components in the mode generation and detection process without inducing extra optical aberrations. The resolution of correction phase map doesn't limit by the grating size which diffract the beam to interfere. The phase correction map describes the real phase difference caused by optical aberrations thus is unique and stable. The phase correction map doesn't depend on any initial value and is also mode independent and works for all OAM modes. We will describe this method in detail in the next section.

3.3 Correction of beam distortion

Phase error correction is critical for preparation and measurement of light in well-defined transverse spatial modes, which can be used to encode and transmit information. In our experimental approach, we use phase-only SLMs for state preparation and state detection of light carrying OAM in LG modes. To construct the described system aberrations, we need to extract the phase error caused both by the SLM and optical elements in the optical system. This phase map can then be used to perform aberration correction by implementing the inverse phase map transformation with the SLMs. In a simplified experimental scheme shown in Fig. 3.1, this is achieved by using the SLM as a grating to diffract different regions of the input beam and let the beams come from two different regions interfere. This interference provides information about the relative phase between the two regions. By observing the inferference of different regions of the SLM with a specific, fixed region used as a

phase reference, it is possible to reconstruct the map of relative phases among regions of the SLM, which can be used to infer the distortion of the incoming beam. The phase error correction method that we use in our experiment follows the work in [67]. For a simplified case which only need to correct the wavefront distortion caused by the input beam deviation from Gaussian, a SLM and a Fourier lens, the experiment set up is showed in Fig. 3.1.

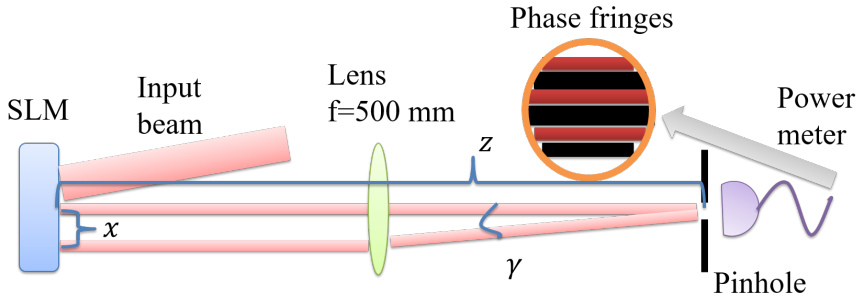

Figure 3.1: Simplified setup: The SLM is illuminated by a collimated beam. The beam is reflected by two patches of grating on the SLM and focused on the image plane by a Fourier lens. We set a 30μm pinhole on the focal point and a power meter after the pinhole.

The SLM is illuminated by a collimated beam with a beam diameter of 0.6cm, which covers the most area of the 600×792 pixels SLM. The light is diffracted into the first order diffraction mode by a diffraction grating encoded on the SLM and focused on the image plane by a Fourier lens, as shown in Fig. 3.1. In this scheme, we encode a small square diffraction grating on the SLM in the region coinciding with the center of the incoming beam. This is a small patch grating referred to as reference grating and with the size of 18×20 pixels, each pixel is 20μm by 20μm. In this method a second grating, called a sample grating of the same size as the reference grating, is generated on another region of the SLM which is also illuminated by the input beam. Thus for the input beam, only the two parts incident in these two small regions are diffracted by the SLM, one part is on the beam center, the other part is on the outer region, as shown in Fig. 3.1. The interference of the two regions in the Fourier plane results in interference fringes and provides information about the relative phase between the two regions of the beam. By scanning the second region

over the spatial extend of the light beam on the SLM while keeping the reference grating constant and observing the interference between these two fractions of the incident beam, it is possible to obtain phase distortion information of the optical system over the beam spatial extend [67]. This method of scanning the sample grating is illustrated in Fig. 3.2.

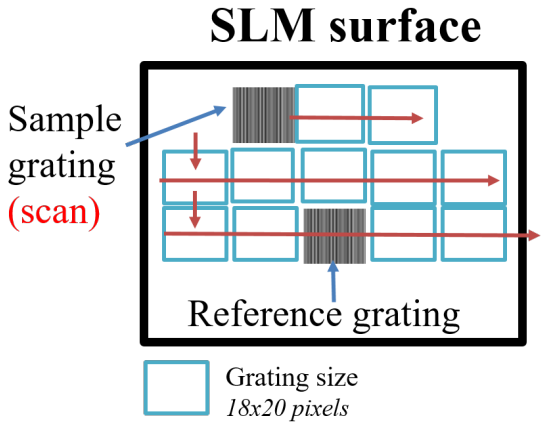

Figure 3.2: The reference grating is on the center of the SLM and the sampling grating scans over the area covered by the incoming beam.

After passing through the Fourier lens, the diffracted first order mode will interfere on the focal point on the image plane. We set a 30μm pinhole at the focal point and a power meter after the pinhole to detect the intensity at a point of the interference fringes while changing the relative phase between the reference grating and the sample grating. The beam diffracted by the reference grating on the focal plane can be described by:

$$E_{ref} = ae^{ikz} \tag{3.2}$$

with amplitude a, the wave vector $k = \frac{2\pi}{\lambda}$, and the distance z from the SLM surface to the focal point. Similarly, the sample beam can be described by:

$$E_{samp} = be^{i(kz-\Delta\phi)} \tag{3.3}$$

with b representing the amplitude of the diffracted sampling beam and $\Delta\phi$ is the phase difference including the phase difference caused by γ and the phase aberration

due to the SLM and the lens. γ is the intersection angle between the two beams diffracted by the sample and reference grating after the Fourier lens. The intensity of the interference pattern at the Fourier plane of the lens is then given by:

$$I = |E_{ref} + E_{samp}|^2 = a^2 + b^2 + 2ab\cos(\Delta\phi) \tag{3.4}$$

To retrieve the phase difference $\Delta\phi$ which describes the phase distortion over the illuminated area on the SLM by the incoming beam, we need to scan the sample grating to cover the whole area of the incoming beam three times with the reference grating maintaining the same phase and the sample grating with a $\frac{2\pi}{3}$ phase step increment each time. Thus in each step during the process of sample grating scanning, the phase of the sample grating takes the following values: $0, \frac{2\pi}{3}, \frac{4\pi}{3}$. Then the sample beam in each scanning step becomes:

$$E^q_{samp} = be^{i(kz-\Delta\phi+q(\frac{2\pi}{3}))} \tag{3.5}$$

with $q = 0, 1, 2$ and the interference intensity after the pinhole is:

$$I_q = |E_{ref} + E^q_{samp}|^2 = a^2 + b^2 + 2ab\cos(\Delta\phi - q(\frac{2\pi}{3})) \tag{3.6}$$

From three intensity measurements with $q = 0, 1, 2$, the phase map can be retrieved by calculating the quantity p defined as:

$$p = \frac{-1}{3}(I_3 + I_2 - 2I_0) + \frac{i}{\sqrt{3}}(I_1 - I_2) \tag{3.7}$$

with

$$\begin{aligned} I_1 &= a^2 + b^2 + 2ab\cos\Delta\phi \\ I_2 &= a^2 + b^2 + 2ab\cos(\Delta\phi - \frac{2\pi}{3}) \\ I_3 &= a^2 + b^2 + 2ab\cos(\Delta\phi - \frac{4\pi}{3}) \end{aligned} \tag{3.8}$$

so that the phase error at a given point in the (x, y) transverse plane equals:

$$\Delta\phi = arg(p) \tag{3.9}$$

and:

$$2ab = |p| \tag{3.10}$$

The interference pattern obtained on the focal plane by scanning the sample grating corresponds to fringes with periodicity $\frac{\lambda}{\sin\beta}$. λ represents the laser wavelength, and β is the smallest intersection angle between the two diffracted beams, namely the smallest γ. The interference fringes can be detected at the origin using a point detector, such as a detector behind a pinhole or a small region on an image sensor [76]. By setting a 30μm pinhole before a power meter, we can obtain the interference intensity of a particular point. The pinhole size should be smaller than the smallest interference period expected for the setup, $\frac{\lambda}{\sin\beta}$, and the angle β could be estimated as the ratio of the size of the reference grating divided by the focal lens.

To get a smooth phase map to be used for aberration correction, we make use of oversampling. For a sample grating of size 18×20, the displacement of the sampling grating is performed in steps of 5 pixels in the x or y direction each time. This oversampled array allows us to take linear interpolation to get a full phase map which matches the size of the SLM screen.

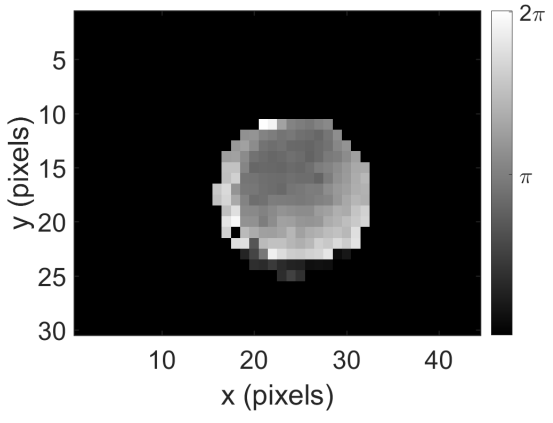

Figure 3.3: Phase map data matrix without oversampling procedure. Note that the phase map is pixelated and the relatively large phase changes among consecutive pixels make the process of phase unwrapping to break.

Figure 3.3 shows the phase map obtained by directly shifting the sampling patch in steps equal to the size of this patch to cover the whole beam without overlapping.

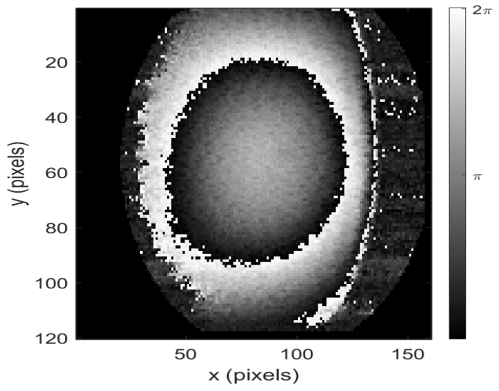

Figure 3.4: phase map data matrix with oversample method.

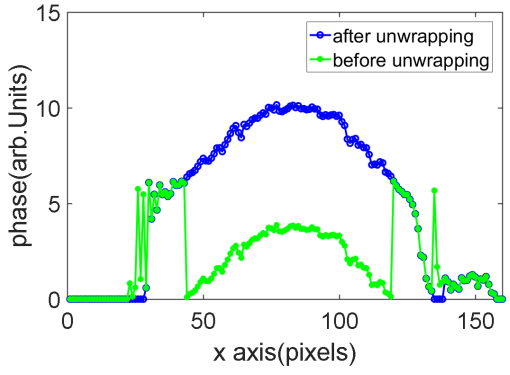

Figure 3.5: Sample of phase map for different values of x for a fixed y pixel,which is a horizontal cut of the phase map matrix at $y = 0$. The green dots are the wrapped phase value and the blue dots represent the phase value after unwrapping.

It is pixelated and does not allow to retrieve a continous phase map. Figure 3.4 depicts the oversampled phase map. This map contains many more data points which allow to perform a good linear interpolation between those points to construct the full phase map with relatively low background noise ratio. The obtained data usually shows discrete jumps of 2π in phase as discontinuities in the phase map. We use a phase unwrapping method to get rid of the apparent phase discontinuity on the phase map, similar to [75]. The phase discontinuity appears in our aberration correction map because it is obtained using the function $arg(p)$, which projects all the phase values to the range of phases $(-\pi, \pi]$. In cases where the phase exceeds the range of $(-\pi, \pi]$, it would contain more than 2π jumps between the two consecutive points.

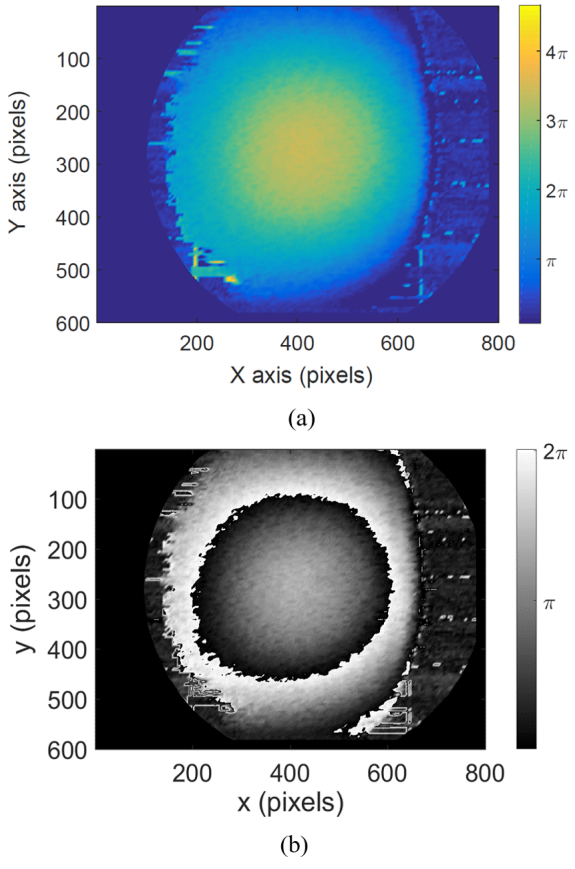

Figure 3.6: (a): phase map after unwrapping and linear interpolation. (b): hologram obtained by mapping the phase map into a 2π range.

Thus, correct phase relations between neighboring sample points need to be found prior to interpolation. This process is called phase unwrapping.

Figure 3.5 illustrates a horizontal cut of the phase map matrix before and after unwrapping. Multiples of 2π are added to the adjoint points when absolute jumps between consecutive points are greater than or equal to the default jump tolerance of π radians. The oversampling method also confirms the phase difference between adjacent points is no bigger than π. At the edges of the matrix points corresponding to the boundaries of the light beam, the phase unwrapping method tends to give nonconsistent answers and incorrect phase shifts. This effect is due to the low intensity at the edges of the beam compared to the background, the large observed intensity fluctuations in these regions. In these situations, we define the phase values at certain points where the large intensity fluctuations produce unphysical spikes and

phase jumps to the average level around these points. This step is performed by a discrimination procedure done in an automatic manner in our analysis. Thus we get a fluent phase map and the LG mode intensity pattern is stable when generated by the phase map after time pass. After the correction for unphysical phase spikes and applying the phase unwrapping procedure, we perform a linear interpolation to construct a full phase map which can be encoded into the SLM for aberration correction. The full phase map corrects for the SLM's flatness and compensate for the aberrations of the other optical elements in the system. The final phase map and the hologram that is encoded in the SLM for aberration correction are shown in Fig. 3.6.

The phase error correction beam shaping method allows for accurate generation of LG modes. Using this method, we investigate the improvement of phase detection and aberration correction for the preparation of different LG modes at different mode orders. For this investigation, we use the experimental setup that has been described in Chapter 2 and Fig. 3.8 for the generation of LG modes with and without aberration correction. For aberration correction, the correction map is added to the hologram encoded in the SLM for the generation of different modes. Figure 3.7 shows examples for the preparation of different OAM modes with different orders with and without aberration correciton. The SLM encodes a hologram corresponding to a LG mode and the image is observed on the focal plane taken via a CCD camera. Comparison of the different LG modes with different OAM orders, modes before and after adding the phase aberration correction map $\Delta\phi$ to the SLM show the improvement in the intensity pattern. We can observe that while the uncorrected fundamental ($l = 0$) Gaussian mode shows some degree of ellipticity, the corrected mode is closer to a 2D Gaussian intensity distribution. It improves the OAM modes quality in the preparation process. We note that the highest dimension we can reach for LG modes with good quality depends on the size of the LG mode beam waist used to generate the hologram, comparing with the phase correction map size, and the distortions in the edges of the map. In general, the phase map edge deviates more from the real phase map than the center part, and this limits the performance for phase correction

and state preparation for OAM modes. Figure 3.7 shows the preparation of OAM modes in different orders with and without correction showing a good improvement even at high l, e.g., $l = 8$.

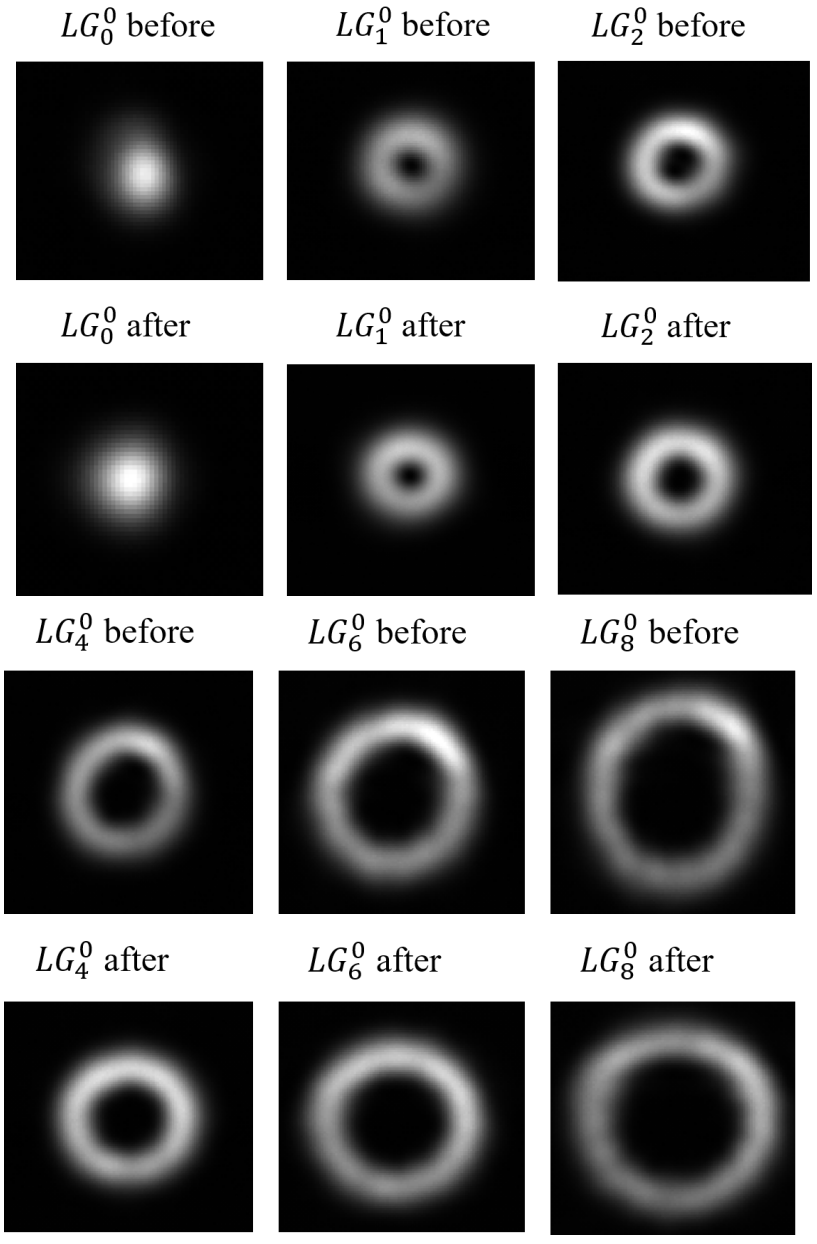

Figure 3.7: Beam shaping performance before and after applying the phase map correction for different LG modes with the image taken on the Fourier plane of the lens F3.

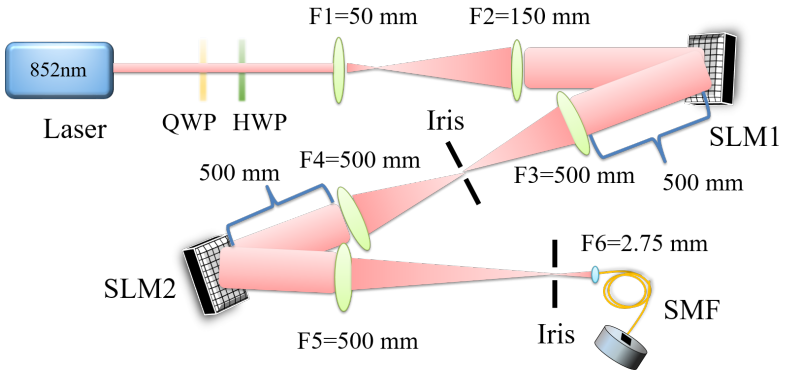

Figure 3.8: Experimental setup. SLM1 is imaged on SLM2 by a 4f-system with an iris on the focal plane of lens F3. By encoding SLM2 with a conjugate mode of the mode generated by SLM1, the mode generated can be project into a LG_0^0 mode, which overlaps with the fundamental mode of the fiber and can be coupled into the single mode fiber.

This aberration correction method can not only be applied to increase the quality for state preparation but also can be applied to improve state detection of OAM states based on SLMs. Using a SLM (SLM1) for state preparation, a second SLM (SLM2) can be used to perform projective measurements, as shown in Fig. 3.8. After state preparation with SLM1, the mode can be imaged onto SLM2 by using a 4f-system. The SLM2 converts the LG modes generated by SLM1 to the LG_0^0, which has a high overlap with the fundamental mode of single mode fiber, thus can be coupled into the single mode fiber. In our experiment, we first correct for the aberration caused by SLM1, lens F1, lens F2 and lens F3 by setting the pinhole at the Fourier plane of lens F3 and scanning the grating patch to get the phase correction map for state preparation (map1). Then, we add the phase correction map map1 on SLM1 and obtain the phase correction map for state projection (map2) for lens F4, SLM2 and lens F5 by locating a pinhole on the focal plane of lens F5, following the same procedure for phase correction. After adding the phase correction map2 on SLM2, we correct for almost all the aberrations caused by the optics in our experiment. The results for aberration correction show in Fig. 3.9. By applying the phase map map1 and map2, we can generate and detect LG modes in high quality.

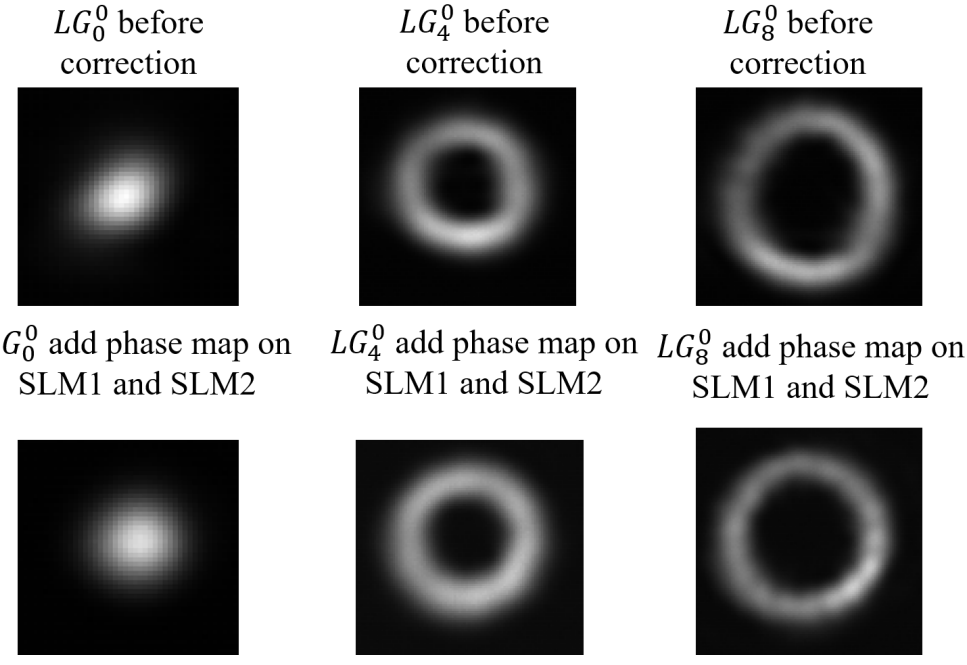

Figure 3.9: Beam shaping performance before and after applying the phase map correction for different LG modes. The hologram encoded the LG mode is added on SLM1. We get the distorted LG modes without any phase correction and add the phase map corrections for the two SLMs to get the improved LG modes.

3.4 Conclusions

LG modes are very sensitive to optical aberrations. In this chapter, we investigated a method for aberration correction based on beam interference to extract the phase map that represents the aberrations of the optical system including all optical components. By using the method, the obtained phase map can be used to correct for all the aberrations. We applied the obtained phase correction maps to the two SLMs for the LG modes generation and the detection process. We observed this aberration correction method allowed for increasing the quality of the preparation of optical modes with high OAM order l. This method can also be applied to the operation used for state projection to improve the performance for projection and detection of states of light in LG modes.

Chapter 4

OAM normalization in mode generation and detection process

The investigation of protocols for quantum state tomography requires methods for state preparation and measurement of OAM states in high dimensions with high fidelity and good efficiency. In this chapter, we investigate the efficiency of the beam shaping method for preparing states of light in OAM modes and in superpositions of OAM states with different OAM order, and projective measurements implemented by mode conversion and detection using SLMs and a single mode fiber (SMF). The SMF works as a spatial mode filter that mainly transmits the fundamental Laguerre Gaussian (LG_0^0) mode, which has large overlap with the fundamental mode of the fiber. We find that the efficiencies for the generation and projection of modes with spatial information using SLMs are mode dependent. We also find that efficiency calibration and compensation are essential for achieving good performance for state preparation and state measurement for future investigations of quantum state tomography protocols.

4.1 State preparation for photons with OAM

As investigated in the previous chapters, the methods for aberration correction based on beam shaping techniques with SLMs can allow for the generation and detection of OAM or LG modes with high quality. However, the efficiency of the generation of light with OAM and the efficiency of projective measurement depend strongly on the specific LG mode that is prepared and detected. Moreover, this dependence substantially degrades the performance of state preparation and projection when generate and detect more complicated states, such as superpositions of LG modes with different mode order l.

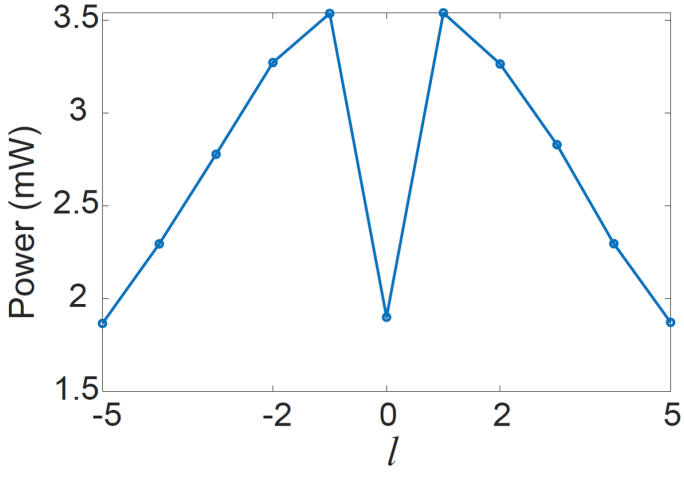

Figure 4.1: Intensity of the generated modes with different OAM order l. The LG modes generated by SLM1 change the mode order l from $l = -5$ to $l = 5$. The first order mode diffracted by the phase grating is selected and the power of the generated LG mode varies when the mode order l changes.

For LG modes generated by the first SLM (SLM1) with the state preparation method mentioned in Chapter 2, the intensity of OAM mode varies when the mode order l changes. The generation efficiency of LG modes decreases when the OAM mode order increases, and the LG_0^0 mode has an unexpectedly low generation efficiency, as shown in Fig. 4.1. The unequal mode generation efficiencies indicate that the superpositions of different LG modes have different generation efficiencies. A general approach to solve this problem is to make different LG modes to have the same

generation efficiency, namely normalizing the generated LG modes. The normalization procedure can be achieved by modifying the phase grating depth for each LG_l^0 mode, thus modifying the intensity of the OAM mode which is diffracted by the phase grating. The efficiency of the generated LG mode depends on the Taylor Fourier expansion coefficient in Eq. (2.13) with parameters M and H from Eq. (2.14). We describe the LG mode used to generate the hologram encoded in SLM1 as:

$$\mathrm{LG}_l^0 = A_l e^{i\Phi_l} \tag{4.1}$$

where A_l is the LG mode amplitude, and Φ_l is the phase of the LG mode. The LG mode generated and detected in the Fourier plane is described as $|l\rangle$. The first order Taylor Fourier coefficient shows that the intensity of the generated LG mode $|l\rangle$ has a linear relationship with the intensity of the LG mode $|A_l|^2$ used to generate the hologram. To normalize the LG modes, we choose to lower the generation efficiency of LG modes down to the lowest value of the generation efficiency among all LG modes. The mode generation efficiency can be linearly lowered by multiplying a normalization factor to the intensity $|A_l|^2$ of each LG mode which is used in the process of generation of hologram. The normalization factor $Norm(l)$ is obtained by using the minimum intensity of the generated LG mode dividing the intensity of each generated mode accordingly. For example, the normalization factor $Norm(3)$ for mode LG_3^0, $|l = 3\rangle$ is obtained by the generated intensity of mode $|l = 5\rangle$ divided by the generated intensity of mode $|l = 3\rangle$ while generating the LG mode with OAM order changing from $l = -5$ to $l = 5$.

In our experiment, the intensity of the LG mode ($|l\rangle$) prepared doesn't change strictly linearly when varies the intensity ($|A_l|^2$) which is used to generate the hologram in SLM1. Suppose the relative weight $P(i)$ is a viable changes from 0 to 1, and we use the intensity $|A_l|^2$ of LG mode times $P(i)$ to generate the hologram. The relation between the intensity of the prepared LG mode and $P(i)$ is illustrated in Fig. 4.2.

We use an iterative method to solve this nonlinearity problem. Suppose the initial hologram encodes the mode LG_l^0 in the iterative procedure. To achieve uniform generation efficiency of LG mode $|l\rangle$, we first encode the LG mode LG_l^0 in the hologram

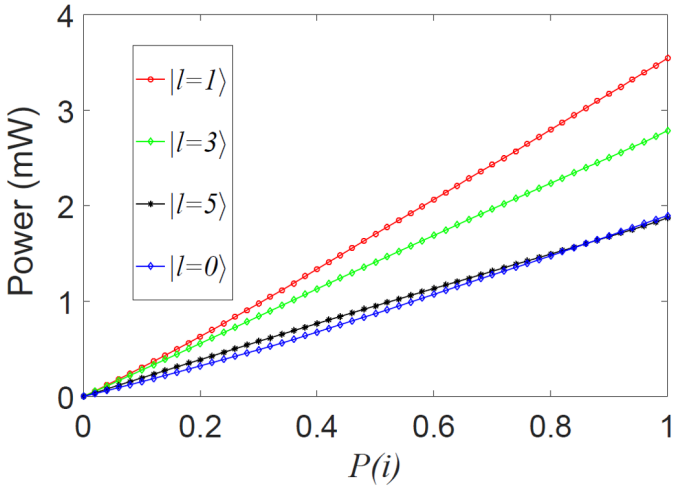

Figure 4.2: Nonlinear relation between the mode intensity used to generate the hologram in SLM1 and the power of the generated LG mode. The intensity of $|l = 1\rangle$ (red line), $|l = 3\rangle$ (green line), $|l = 5\rangle$ (black line) and $|l = 0\rangle$ (blue line) mode varies as linearly changing relative weight $P(i)$ used in hologram generation. $P(i)$ changes from 0 to 1. The hologram used in the mode preparing procedure is obtained by $P(i)$ times the LG mode intensity.

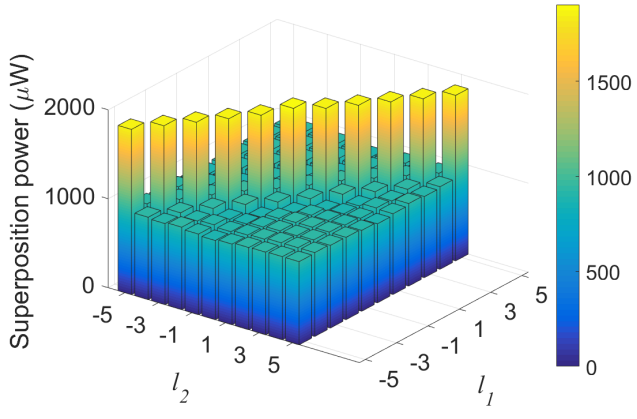

Figure 4.3: Generation power of the normalized LG modes. The two horizontal axes represent mode order l_1 and l_2 changing from -5 to 5. The vertical axis represents the generation power of LG mode superposition when generating $0.5|l_1\rangle + 0.5|l_2\rangle$ by SLM1.

in SLM1 by:

$$\mathrm{LG}_l^0 / max(|A_l|) \tag{4.2}$$

where max picks the maximum value of the amplitude pattern $|A_l|$ of the desired LG

mode. Then obtain the normalization factor $Norm(l)$ in the first iteration. After obtaining the normalization factor $Norm(l)$, we encode the hologram with the LG mode of the form $\mathrm{LG}_l^0/max(|A_l|)\cdot\sqrt{Norm(l)}$, detect the generation intensity of the LG mode and update normalization factor in the next iteration. The normalization factor is updated by multiplying the initial normalization factor with the updated normalization factor obtained in the next iteration. The LG modes can be normalized by using the normalization factors obtained after a few iterative loops to generate the hologram.

The diagonal terms of the matrix in Fig. 4.3 shows the normalized $|l\rangle$ modes, with equal intensity for each LG mode. Since the $|l=0\rangle$ mode intensity is much lower than other modes, we ignore $|l=0\rangle$ and normalize among other LG modes. In the normalization process for generated LG mode, we normalize the generation efficiency based on $|l=5\rangle$. The mode generation efficiency after normalization is 19.98%. In fact, the same normalization factors can be applied to generate superpositions of LG modes and obtain uniform intensity when mode order l varies, as shown in the off diagonal terms in Fig. 4.3. To obtain uniform generation efficiency with superpositions of LG modes, the superposition of LG modes with the normalization factors, which is used to generate the hologram, should be:

$$\sum_l P(l)e^{i\Omega_l}\mathrm{LG}_l^0/max(|A_l|)\cdot\sqrt{Norm(l)} \tag{4.3}$$

where $P(l)$ is the relative weight of superposition for each $|l\rangle$ and should sum to 1. $Norm(l)$ is the normalization factor and Ω_l is the relative phase. We obtain uniform generation power of LG mode superposition as shown in the off diagonal terms of the matrix in Fig. 4.3. The value of $P(l)$ influences the generation efficiency of LG mode superposition. Suppose the value of $P(l_1=1)$ varies as $P(i)$, which also varies from 0 to 1, the generation efficiency of LG mode superposition changes with $P(l_1=1)$ is shown in Fig. 4.4. The dimension of the LG mode superposition also affects the minimum intensity that mode generation can reach. These limit the measurement protocols that can be tested in this experimental platform. The relative phase Ω_l between each LG_l^0 mode in the superposition doesn't influence the generation intensity of the superposition.

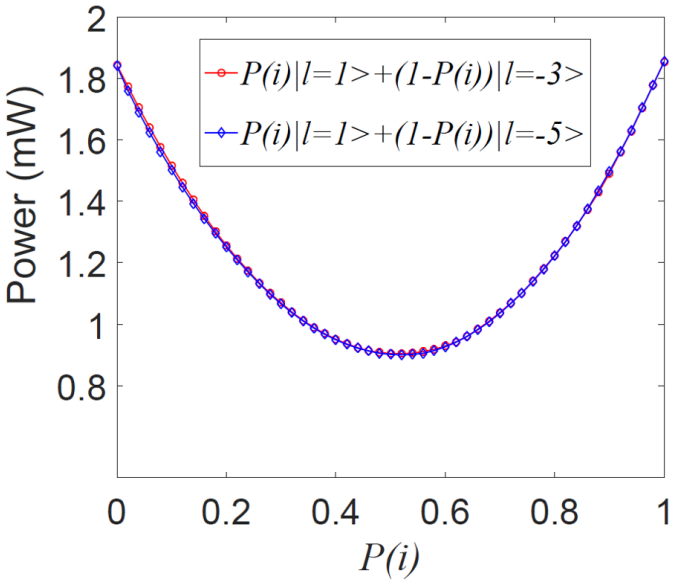

Figure 4.4: Measured power of LG superpositions as a function of relative weight $P(i)$ changes in two LG mode generation process. The two generated LG modes are $P(i)|l=1\rangle + (1-P(i))|l=-5\rangle$ and $P(i)|l=1\rangle + (1-P(i))|l=-3\rangle$. These superpositions of LG mode are generated by SLM1.

4.2 Projective measurements of OAM modes

We normalize the generation efficiency for different LG mode in the above section. The efficiencies obtained by different LG modes projective measurement also need to be normalized since the projection efficiencies depend on the LG mode which is used to perform the measurement. The experimental procedure for the projective measurement of LG modes is described in Chapter 2. The intensity distributions of the projections of LG modes at the transverse Fourier plane are shown in Fig. 4.5, which are also the intensity distribution at the SMF facet. The mode resulting from the conjugate transformation performed by the SLM2 has large overlap with the fundamental mode of the fiber and can be coupled into the SMF. The radius and the intensity of the mode on the Fourier plane after projective measurement decrease when the orbital angular momentum number l increases. Thus we maximize the coupling efficiency of the mode which has the smallest radius on the Fourier plane

after projective measurement. For example, when OAM mode order changing from $l = -5$ to $l = 5$, we maximize the coupling efficiency for the mode $|l = 5\rangle$.

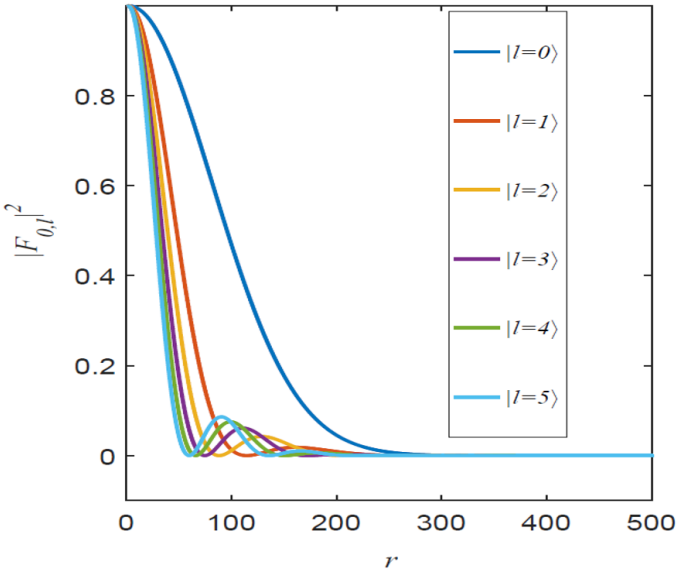

Figure 4.5: Intensity distribution of $|\mathcal{F}_{0,l}|^2$ at the Fourier plane of SLM2. The intensity distributions of LG modes are obtained by the projective measurements with OAM mode order $l = 0, 1 \cdots 5$. The figure comes from [1].

We can normalize the efficiency for LG_l^0 mode projective measurement after maximizing the coupling efficiency for the projection of mode $|l = 5\rangle$. The mode obtained by the LG mode projective measurement is coupled into the SMF when LG_l^0 modes vary from $l = -5$ to $l = 5$, as shown in Fig. 4.6. The input-output matrix describes the power obtained by performing different projective measurements. The non-normalized input-output matrix is shown in Fig. 4.6, which indicates that different LG modes have different projection efficiency when the mode generation efficiency is the same. By using the iterative method we described in the section above, we can find the normalization factors for the holograms encoded on SLM2 to normalize the projection efficiency for different LG_l^0 modes, as shown in Fig. 4.7. We set the fiber and the coupling lens by maximizing the coupling efficiency of the projective measurement for $|l = 5\rangle$. The projection efficiencies of LG modes are normalized according to the projection efficiency of $|l = 1\rangle$. As shown in Fig. 4.7, the LG modes with mode order l varying from $l = -5$ to $l = 5$ have the same coupling efficiency for the projective measurement. For example, for the detection process

of $|l = 5\rangle$, the diffraction efficiency of mode $|l = 5\rangle$ is 29.44% when the mode is diffracted by the phase grating encoded on SLM2. The coupling efficiency of the projective measurement for mode $|l = 5\rangle$ is 25.67%. The efficiency of the projective measurement including the process of the beam diffracted by SLM2 and coupled into the SMF for all normalized LG modes is 7.53% when mode order l changes from $l = -5$ to $l = 5$. As a result, the total efficiency containing mode generation and projection process for all normalize LG modes is 1.51%.

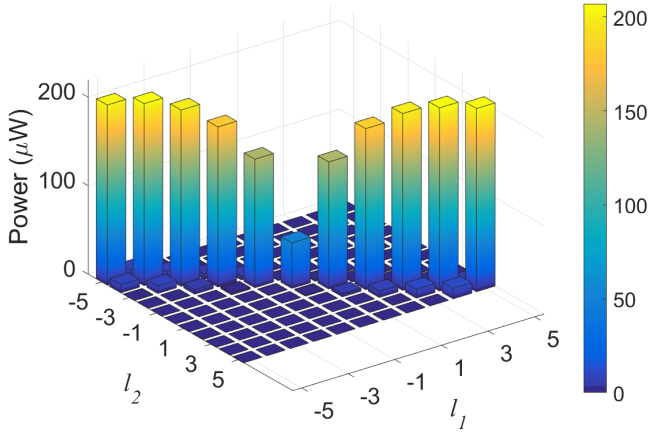

Figure 4.6: Non-normalized input-output mode matrix of projective measurements for LG modes ranging from $l = -5$ to $l = 5$. The vertical axis shows the power measured by performing the projection of the LG mode $|l_1\rangle$ generated by SLM1 onto the mode $\langle l_2|$ implemented by the mode transformation with SLM2 and mode projection with the SMF. The coupling power into the SMF is maximized by the projective measurement of mode $|l = 5\rangle$.

We use visibility to describe the crosstalk in the normalized input-output matrix obtained by the projective measurement, as shown in Fig. 4.7. The visibility is defined as the sum of the diagonal terms of the input-output matrix divide by the sum of all input-output matrix elements [77]:

$$V = \sum_{i} C_{ii} / \sum_{ij} C_{ij} \tag{4.4}$$

where C_{ij} corresponds to the input-output matrix element. The visibility of the normalized input-output matrix is 95.36%. Figure 4.8 shows the input-output matrix obtained by optimizing the coupling efficiency of $|l = 10\rangle$ in the projective measure-

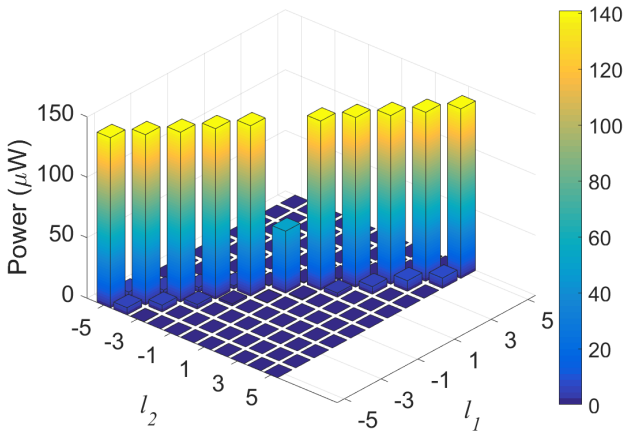

Figure 4.7: Normalized input-output mode matrix of projective measurements for LG mode ranging from $l = -5$ to $l = 5$. The vertical axis shows the power measured by performing the projection of the LG mode $|l_1\rangle$ generated by SLM1 onto the mode $\langle l_2|$ implemented by SLM2 and mode projection with the SMF. The coupling power into the SMF is maximized by the projective measurement of mode $|l = 5\rangle$.

ment process, compared with Fig. 4.7, which shows the input-output matrix obtained by optimizing the coupling efficiency of the projection of $|l = 5\rangle$. There are more overlaps of the off diagonal elements in the input-output matrix while maximizing the coupling efficiency of the projection of $|l = 10\rangle$, and the visibility is 88.60%, lower than optimizing the coupling efficiency of the projection of $|l = 5\rangle$.

We can use a CCD for the projective measurement instead of coupling the mode into a SMF. The same normalization factors are obtained by using a CCD to detect the center intensity of mode which is projected on the Fourier plane, comparing with measuring the power of the mode coupled into the fiber. The center intensity of the projective measurement of mode $|l = 5\rangle$ is the area to measure in both cases.

As for projective measurement of LG modes in superpositions, the detection efficiencies are different for different superpositions. The superposition of LG modes should in a form as:

$$\sum_l P(l) e^{i\Omega} \mathrm{LG}_l^0 / max(|A_l|) \cdot \sqrt{Norm(l)} \tag{4.5}$$

with $\sum_l P(l) = 1$ to generate the hologram encoded on SLM1 and use the conjugate

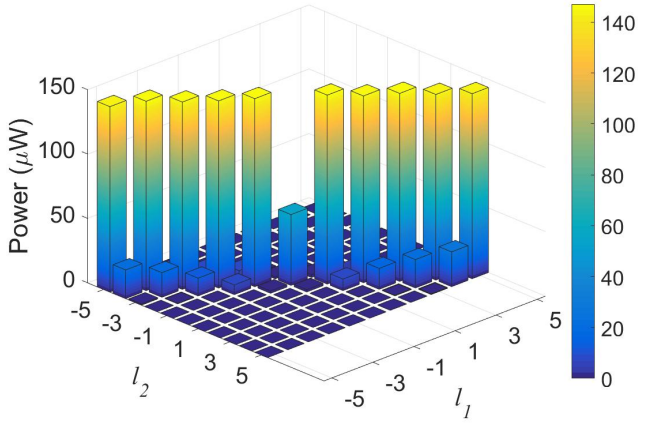

Figure 4.8: Input-output mode matrix of projective measurements for $|l\rangle$ mode with normalization. The vertical axis shows the power measured by performing the projection of the LG mode $|l_1\rangle$ generated by SLM1 onto the mode $\langle l_2|$ implemented by SLM2 and mode projection with the SMF. The mode order l changes with $l = -5, -4, \cdots, 5$. The coupling power into the SMF is maximized by the projective measurement of mode $|l = 10\rangle$.

form to generate the hologram encoded on SLM2. Different normalization factors should be applied to holograms encoded on SLM1 and SLM2, corresponding to the LG mode generation and detection process. The projection efficiency is equal when detect superposition of LG modes with different OAM mode order l and equal relative weight $P(l) = 0.5$, as shown in Fig. 4.9. The equal projective efficiency of normalized LG mode superposition allows us to test certain measurement protocols in state tomography, e.g., using MUB to reconstruct the density matrix. However, the efficiency of the projective measurement changes when the relative weight $P(l)$ of the superposition of LG mode changes, as shown in Fig. 4.10, in which $P(1)$ is represented by the viable $P(i)$. The lowest projection efficiency of superpositions of LG modes is obtained when the relative weight $P(l)$ of the superpositions are equal for different mode order l. This is illustrated in Fig. 4.10. The efficiency of projective measurement, which depends on the relative weight $P(l)$, limits the possible POVMs that could be tested with the experimental setup for state tomography.

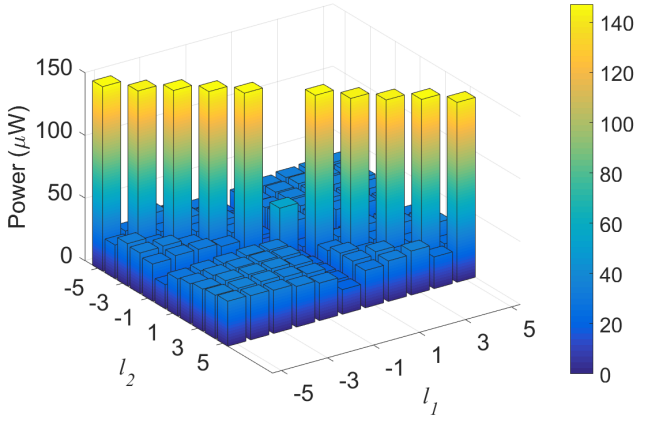

Figure 4.9: Measured output power coupled into the SMF of LG mode superposition. SLM1 generates mode $0.5|l_1\rangle + 0.5|l_2\rangle$ and the mode is imaged onto SLM2 by the 4f-system, which encodes $0.5\langle l_1| + 0.5\langle l_2|$. The mode orders l_1 and l_2 change from -5 to 5. The two horizontal axes represent l_1 and l_2, and vertical axis represents the power of projective measurement.

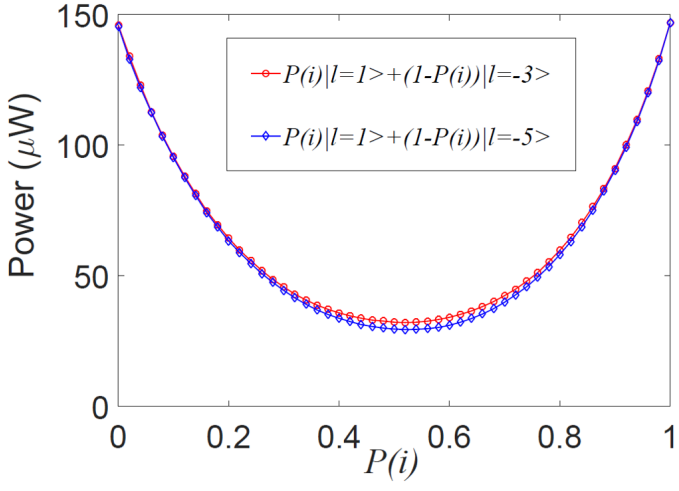

Figure 4.10: Power coupled into the SMF obtained by LG modes projection. SLM1 generates mode $P(i)|l_1\rangle + (1-P(i))|l_2\rangle$ and the mode is imaged onto SLM2 by the 4f-system, which encodes $P(i)\langle 1_1| + (1-P(i)\langle l_2|$ with the relative weight $P(i)$ changes from 0 to 1.

Figure 4.11 shows the coupling power of projective measurements when we change the relative phase of the superposition of LG modes encoded on SLM2. We also find that the projection efficiency of LG mode decreases when the dimension of superposition of LG mode increases. The low efficiency of the projective measurement

of LG mode superposition in high dimensions also limits the possible measurement protocols that could be applied to the experimental platform.

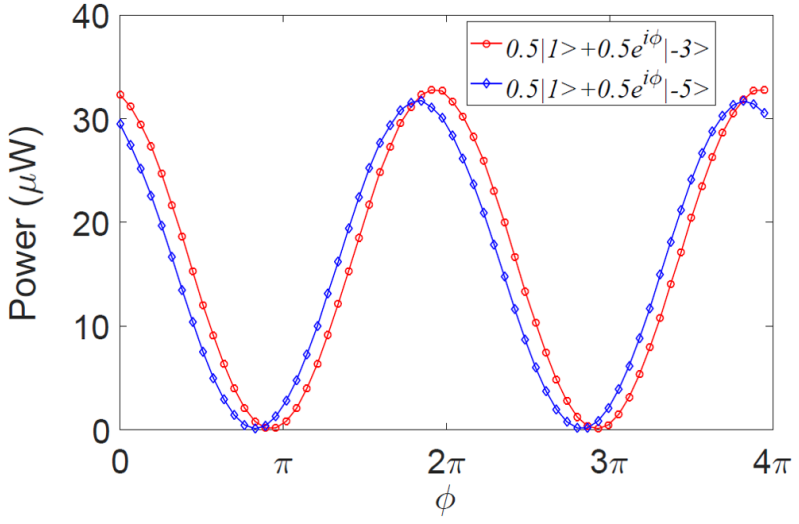

Figure 4.11: Power coupled into SMF obtained by projection of LG modes. SLM1 generates mode $0.5|l=1\rangle + 0.5|l=-3\rangle$ and $0.5|l=1\rangle + 0.5|l=-5\rangle$ in different mode generation process. These two mode are imaged on SLM2 by the 4f-system, which generates $0.5\langle l=1| + e^{i-\phi}0.5\langle l=-3|$ and $0.5\langle l=1| + e^{i-\phi}0.5\langle l=-5|$ with the relative phase ϕ changing.

The MUBs consist of $d+1$ basis measurements and the overlap between two states among different basis is equal to $1/d$. MUBs are one applicable POVM for our experimental platform for state tomography. Figure 4.12 shows the projective measurements between the MUBs for 2D. The MUBs in 3D are shown in the Tab. 4.1. The MUBs in 2D and 3D as shown in the Tab. 4.1 are not normalized since the experimental setup requires the relative weights sum to 1. Figure 4.13 shows the projective measurements for MUB basis in 3D. The results of projective measurement indicate that the experiment system can be applied to perform state tomography in 2D and 3D.

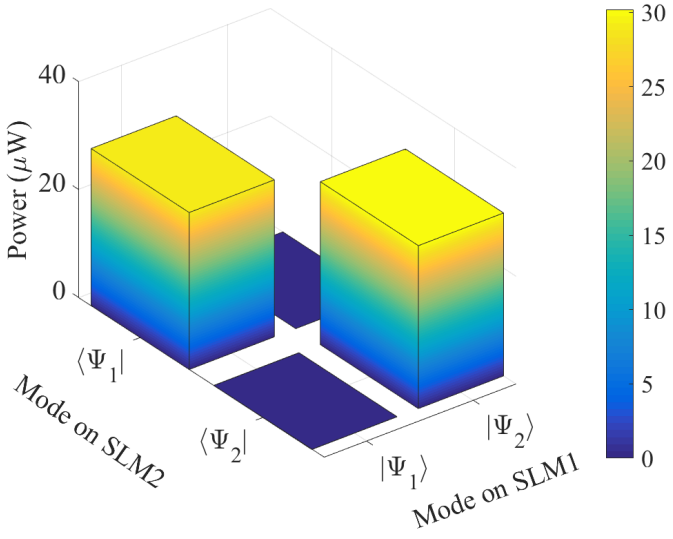

Figure 4.12: Detection power coupled into the SMF after LG modes projection. SLM1 generates $|\Psi_1\rangle$, $|\Psi_2\rangle$ and they are projected on SLM2, which generates $\langle\Psi_1|$, $\langle\Psi_2|$ accordingly. $|\Psi_1\rangle$ is $0.5|l=1\rangle + 0.5|l=-1\rangle$ and $|\Psi_2\rangle$ is $0.5|l=1\rangle - 0.5|l=-1\rangle$.

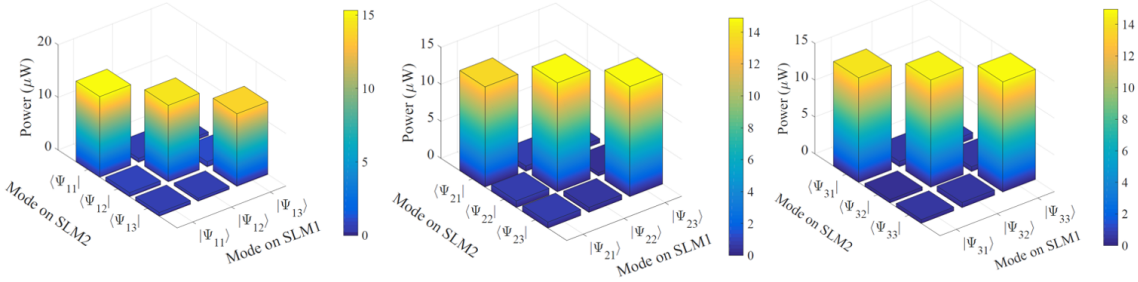

(a) (b) (c)

Figure 4.13: Detection power coupled into the SMF obtained by LG modes projection. (a): SLM1 generates $|\Psi_{11}\rangle$, $|\Psi_{12}\rangle$, $|\Psi_{13}\rangle$ and these modes are projected on SLM2, which generates $\langle\Psi_{11}|$, $\langle\Psi_{12}|$, $\langle\Psi_{13}|$. (b): SLM1 generates $|\Psi_{21}\rangle$, $|\Psi_{22}\rangle$, $|\Psi_{23}\rangle$ and they are projected on SLM2, which generates $\langle\Psi_{21}|$, $\langle\Psi_{22}|$, $\langle\Psi_{23}|$. (c): SLM1 generates $|\Psi_{31}\rangle$, $|\Psi_{32}\rangle$, $|\Psi_{33}\rangle$ and are projected on SLM2, which generates $\langle\Psi_{31}|$, $\langle\Psi_{32}|$, $\langle\Psi_{33}|$. The projective measurements are based on MUBs as shown in Table. 4.1

m	j	
1	$\|\Psi_{11}\rangle$	$\frac{1}{3}\|l=1\rangle+\frac{1}{3}\|l=-1\rangle+\frac{1}{3}\|l=3\rangle$
	$\|\Psi_{12}\rangle$	$\frac{1}{3}\|l=1\rangle+\frac{1}{3}e^{i\frac{2\pi}{3}}\|l=-1\rangle+\frac{1}{3}e^{-i\frac{2\pi}{3}}\|l=3\rangle$
	$\|\Psi_{13}\rangle$	$\frac{1}{3}\|l=1\rangle+\frac{1}{3}e^{-i\frac{2\pi}{3}}\|l=-1\rangle+\frac{1}{3}e^{i\frac{2\pi}{3}}\|l=3\rangle$
2	$\|\Psi_{21}\rangle$	$\frac{1}{3}\|l=1\rangle+\frac{1}{3}e^{i\frac{2\pi}{3}}\|l=-1\rangle+\frac{1}{3}e^{i\frac{2\pi}{3}}\|l=3\rangle$
	$\|\Psi_{22}\rangle$	$\frac{1}{3}\|l=1\rangle+\frac{1}{3}e^{-i\frac{2\pi}{3}}\|l=-1\rangle+\frac{1}{3}\|l=3\rangle$
	$\|\Psi_{23}\rangle$	$\frac{1}{3}\|l=1\rangle+\frac{1}{3}\|l=-1\rangle+\frac{1}{3}e^{-i\frac{2\pi}{3}}\|l=3\rangle$
3	$\|\Psi_{31}\rangle$	$\frac{1}{3}\|l=1\rangle+\frac{1}{3}e^{-i\frac{2\pi}{3}}\|-1\rangle+\frac{1}{3}e^{-i\frac{2\pi}{3}}\|l=3\rangle$
	$\|\Psi_{32}\rangle$	$\frac{1}{3}\|l=1\rangle+\frac{1}{3}\|l=-1\rangle+\frac{1}{3}e^{i\frac{2\pi}{3}}\|l=3\rangle$
	$\|\Psi_{33}\rangle$	$\frac{1}{3}\|l=1\rangle+\frac{1}{3}e^{i\frac{2\pi}{3}}\|l=-1\rangle+\frac{1}{3}\|l=3\rangle$
4	$\|\Psi_{41}\rangle$	$\frac{1}{3}\|l=1\rangle$
	$\|\Psi_{42}\rangle$	$\frac{1}{3}\|l=-1\rangle$
	$\|\Psi_{43}\rangle$	$\frac{1}{3}\|l=3\rangle$

Table 4.1: MUB in 3D. $|\Psi_{mj}\rangle$ denotes the jth element of the mth orthonormal basis of a set of MUBs in 3D. $|\Psi_{mj}\rangle$ satisfies $|\langle\Psi_{mj}|\Psi_{m'j'}\rangle|^2=\frac{1}{9}$ when $m\neq m'$. When $m=m'$, $|\langle\Psi_{mj}|\Psi_{mj'}\rangle|^2=\frac{1}{9}\delta_{j,j'}$. The MUB are not normalized considering the projective measurement we can perform in our platform in 3D.

4.3 Conclusions

In this chapter, we analyse the generation and detection efficiency of LG modes for single LG_l^0 mode and their superpositions. We obtain the normalization factors which can be applied in the LG modes generation and detection process. The normalization factors for each LG_l^0 are obtained by an iterative process. The superposition of LG modes has lower generation and detection efficiency. The projective measurements of the superpositions have the same detection efficiency if we make the LG modes

which compose the superposition with equal relative weight $P(l)$. The low projection efficiency and the request for the equal relative weight of superposition limit the measurement protocols that we can apply by our experimental platform for state tomography. The relative phase change of the LG mode superposition causes a sinusoid power change in the projection process of LG modes. We test the POVM protocols based on MUBs in 2D and 3D, and the results indicate that it is eligible to perform state tomography in our experimental platform.

Chapter 5

Conclusions

The orbital angular moementum (OAM) of photons is a useful degree of freedom with applications ranging from microscopy, imaging, to quantum information. In this thesis, we describe the experimental implementation of a platform which can be used in the future to test different quantum state tomography protocols via photons carrying OAM in high dimensional Hilbert space. Photons carrying OAM that lives in the unbound Hilbert space are able to perform the high-dimensional state tomography. The OAM is caused by the helical wavefront $e^{il\theta}$ of the light. Each photon carries an OAM of $l\hbar$, in which l is the OAM quantum number. We use a holographic beam shaping technique to generate light beam carrying OAM via spatial light modulators (SLMs). The SLMs are beam shaping devices that can change the incident beam phase in 2π radians. The exact solution for OAM beam shaping has been applied to generate the hologram, and thus we can shape both the intensity and the phase of the OAM beam. The beam shaping technique can be applied to shape arbitrary phase and intensity beam profile. We generate the beam carrying OAM by encoding the hologram on the first SLM (SLM1) and observe the OAM modes on the Fourier plane of the Fourier lens. The Gaussian component of the beam can be filtered out by adding a blazed phase grating on the hologram and using an iris on the Fourier plane to pick the first order diffracted mode, which contains the desired OAM mode. We image the OAM mode generated by SLM1 to a second SLM (SLM2) with a 4f-system.

The SLM2 encodes a hologram which is the complex conjugate OAM mode of the mode generated by SLM1, and thus the projective measurement can be accomplished at the far field of SLM2. The projective measurement results in a Gaussian spot which overlaps with the fundamental mode of the fiber, and therefore can be coupled into the SMF.

To generate and detect the OAM modes in high quality, we correct the optical aberrations caused by the SLMs and other optical elements using two beam interference method to get the exact phase map utilizing the SLM. The aberration correction, mainly involving phase distortion, is implemented by interfering two beams diffracted by the two patches of blazed phase grating to obtain the the relative phase difference between these two beams. The phase difference obtained represents the optical aberration, and by subtracting the phase difference, we can produce and detect OAM modes with high quality of OAM mode order $l = 8$.

The generation and detection efficiencies of OAM modes depend on mode order l, and thus we apply different normalization factors of each LG mode on the hologram for both the generation and the detection process to ensure the same efficiency for different LG modes. The normalization factors are obtained by utilizing the linear relation between the intensity of the LG mode used to generate the hologram and the intensity of the mode which is detected on the Fourier plane. We use visibility to describes the crosstalk between the LG modes in the projective measurement process. The visibility of the projection of LG modes is 95.36%, which indicates that the crosstalk is low between different LG modes when taking the projective measurement. The projection efficiency is influenced by the superposition of LG modes, which mainly depends on the relative weight of each LG mode which composes the superposition. The restriction on the value of the relative weight of the LG mode superposition limits the state tomography protocols we can perform in our experimental platform. We take the projective measurements of MUBs in 2 dimensions and 3 dimensions, and verify the orthogonality between the MUBs by using our experimental setup. In general, we can generate and detect LG modes with good quality even with high OAM mode order l. High dimensional quantum states of OAM which are performed

by our experimental platform can be applied to test different POVMs for quantum state tomography in the future research.

Appendix A

Fourier optics and the phase transform function

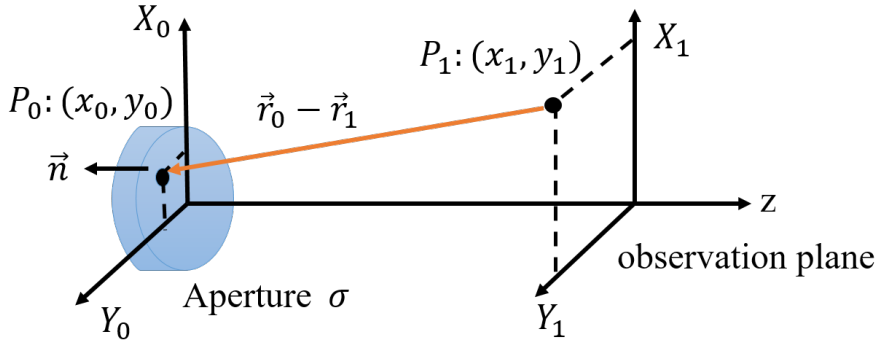

Figure A.1: Light diffraction through an aperture. Point $P_0(x_0, y_0)$ is on the aperture plane and $P_1(x_1, y_1)$ is an arbitrary point on the observation plane. $\vec{n}$ is the normal vector of the aperture.

Diffraction can be defined as any deviation of a light ray from rectilinear propagation, which is not caused by reflection nor refraction. Diffraction theory has been developed by Huygens, Fresnel, Kirchhoff and Sommerfeld [78]. Suppose we want to calculate the electric field in a point P_1 shows in Fig. A.1 after propagation from point P_0. For free space propagation with index of refraction $n = 1$, the electric field E and the magnetic field H of monochromatic light satisfy the Helmholtz equation with wavenumber k:

$$\begin{aligned} \nabla^2\vec{E} + k^2\vec{E} &= 0 \\ \nabla^2\vec{H} + k^2\vec{H} &= 0 \end{aligned} \tag{A.1}$$

We use U to denote the scalar component of the electric field. The field U also satisfies:

$$\nabla^2 U + k^2 U = 0 \tag{A.2}$$

The field on point P_1 after light diffraction through an aperture σ is shown in Fig A.1:

$$U(P_1) = \iint_\sigma h(P_1, P_0) U(P_0) ds_0 \tag{A.3}$$

with $h(P_1, P_0)$ the weighting factor given by the field $U(P_0)$

$$h(P_1, P_0) = \frac{-1}{i\lambda} \cos(\vec{n}, \vec{r}_0 - \vec{r}_1) \frac{e^{-ik|\vec{r}_0 - \vec{r}_1|}}{|\vec{r}_0 - \vec{r}_1|} \tag{A.4}$$

P_0 are all the points on the aperture σ and $U(P_1)$ is obtained by integration over the whole aperture plane σ. $\vec{r}_0 - \vec{r}_1$ is a vector from P_1 to P_0 and $\vec{n}$ is a normal vector to the surface σ. Eq. (A.3) is known as the Rayleigh-Sommerfeld diffraction formula [78]. It shows that the field is a superposition of spherical waves starting from each point in the aperture, each with an appropriate amplitude and obliquity factor $\cos(\vec{n}, \vec{r}_0 - \vec{r}_1)$. This is called the Huygens-Fresnel principle [78]. The aperture lies on a plane (X_0, Y_0) with P_0 of coordinates (x_0, y_0). P_1 with coordinates (x_1, y_1) is on the observation plane (X_1, Y_1), which is parallel to the (X_0, Y_0) plane. So Eq. (A.3) can be written as:

$$U(P_1) = \iint_\sigma h(x_1, y_1, x_0, y_0) U(x_0, y_0) dx_0 dy_0 \tag{A.5}$$

with

$$h(x_1, y_1, x_0, y_0) = \frac{-1}{i\lambda} cos(\vec{n}, \vec{r}_0 - \vec{r}_1) \frac{e^{-ik|\vec{r}_0 - \vec{r}_1|}}{|\vec{r}_0 - \vec{r}_1|} \tag{A.6}$$

and

$$|\vec{r}_0 - \vec{r}_1| = \sqrt{z^2 + (x_0 - x_1)^2 + (y_0 - y_1)^2} \tag{A.7}$$

Suppose the axial propagation distance z is much larger than the aperture size. Then

$$\cos(\vec{n}, \vec{r}_0 - \vec{r}_1) \cong 1 \tag{A.8}$$

and

$$h(x_1, y_1, x_0, y_0) \cong \frac{-1}{i\lambda z} e^{-ik|\vec{r}_0 - \vec{r}_1|} \tag{A.9}$$

therefore $|\vec{r}_0 - \vec{r}_1|$ can be expanded as:

$$\begin{aligned} |\vec{r}_0 - \vec{r}_1| &= \sqrt{z^2 + (x_1 - x_0)^2 + (y_1 - y_0)^2} \\ &\cong z[1 + \frac{1}{2}(\frac{x_1 - x_0}{z})^2 + \frac{1}{2}(\frac{y_1 - y_0}{z})^2] \end{aligned} \tag{A.10}$$

This gives

$$h(x_1, y_1, x_0, y_0) \cong \frac{-e^{-ikz}}{i\lambda z} e^{-\frac{ik}{2z}[(x_1 - x_0)^2 + (y_1 - y_0)^2]} \tag{A.11}$$

When we integrate over the whole plane, we set $U(x_0, y_0) = 0$ outside the aperture and the Eq. (A.5) gives:

$$\begin{aligned} U(x_1, y_1) &= \frac{-e^{-ikz}}{i\lambda z} \iint_{-\infty}^{+\infty} U(x_0, y_0) e^{-\frac{ik}{2z}[(x_1 - x_0)^2 + (y_1 - y_0)^2]} dx_0 dy_0 \\ &= \frac{-e^{-ikz}}{i\lambda z} e^{-\frac{ik}{2z}[x_1^2 + y_1^2]} \iint_{-\infty}^{+\infty} U(x_0, y_0) e^{-\frac{ik}{2z}[x_0^2 + y_0^2]} e^{i\frac{2\pi}{\lambda z}[x_0 x_1 + y_0 y_1]} dx_0 dy_0 \end{aligned} \tag{A.12}$$

This is the Fresnel diffraction integral, which shows that the field $U(x_1, y_1)$ in the observation plane is the 2 dimensional Fourier transform of the field in the object plane

$$U(x_0, y_0) e^{-\frac{ik}{2z}[x_0^2 + y_0^2]} \tag{A.13}$$

with spatial frequencies:

$$f_x = -\frac{x_1}{\lambda z}, f_y = -\frac{y_1}{\lambda z} \tag{A.14}$$

This result is valid close to the aperture, and it is called the near-field approximation [78]. If the distance z satisfies:

$$z \gg \frac{k(x_0^2 + y_0^2)}{2} \tag{A.15}$$

then

$$U(x_1, y_1) = \frac{-e^{-ikz}}{i\lambda z} e^{-\frac{ik}{2z}[x_1^2 + y_1^2]} \iint_{-\infty}^{+\infty} U(x_0, y_0) e^{i\frac{2\pi}{\lambda z}[x_0 x_1 + y_0 y_1]} dx_0 dy_0 \tag{A.16}$$

The region where this equation valid is called the far field or the Fraunhofer diffraction regime [78]. Eq. (A.16) is applied in Eq. (2.2) in Chapter 2.

When a beam passing through a thin lens, it undergoes a phase transformation. The beam leaves the lens surface at the same transverse position (x, y) as where it enters the lens, as shown in Fig. A.2. $U_{11}(x, y)$ is the field incident on the lens, $U_{12}(x, y)$ is the light field leaving the lens and $t(x, y)$ is the phase transform function of the lens, which satisfies:

$$U_{12}(x, y) = t(x, y) U_{11}(x, y) \tag{A.17}$$

the phase transform function $t(x, y)$ of the lens is given by the phase retardation ϕ, with

$$t(x, y) = e^{-i\phi} \tag{A.18}$$

in which

$$\phi(x, y) = kn\Delta(x, y) + k[\Delta_0 - \Delta(x, y)] \tag{A.19}$$

$\Delta(x, y)$ is the thickness between two surface of the lens and Δ_0 is the length of the lens center along z direction with $x = 0$ and $y = 0$. The first term in Eq. (A.19) is the phase variance caused by the beam passing through the lens. The second term is the phase variance between the front incident plane and the back plane of the lens subtracting the phase change caused by the lens. The front surface of the lens has a radius of curvature of $-R_2$ and the radius of curvature of the back surface is R_1. To calculate $\Delta(x, y)$, we split the lens into two parts (Fig. A.2) such that:

$$\Delta(x, y) = \Delta_1(x, y) + \Delta_2(x, y) \tag{A.20}$$

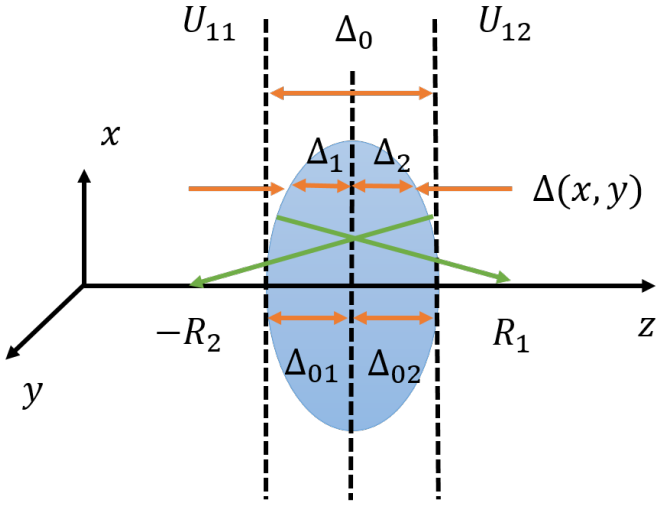

Figure A.2: Parameters of a thin lens. $\Delta(x,y)$ is the lens's thickness between two surface and Δ_0 is the thickness of the lens center. $\Delta_1(x,y), (\Delta_2(x,y))$ is the left (right) thickness of the lens, which satisfies $\Delta_1(x,y) + \Delta_2(x,y) = \Delta(x,y)$. $\Delta_{01}(0,0), (\Delta_{02}(0,0))$ is the left (right) center thickness of the lens, which satisfies $\Delta_{01}(0,0) + \Delta_{02}(0,0) = \Delta_0$.

with

$$\begin{aligned}\Delta_1(x,y) &= \Delta_{01} - (R_1 - (\sqrt{R_1^2 - x^2 - y^2})) \\ &= \Delta_{01} - R_1(1 - \sqrt{1 - \frac{x^2+y^2}{R_1^2}})\end{aligned} \tag{A.21}$$

and

$$\begin{aligned}\Delta_2(x,y) &= \Delta_{02} - (-R_2 - (\sqrt{R_2^2 - x^2 - y^2})) \\ &= \Delta_{02} + R_2(1 - \sqrt{1 - \frac{x^2+y^2}{R_2^2}})\end{aligned} \tag{A.22}$$

thus

$$\Delta(x,y) = \Delta_0 - R_1(1 - \sqrt{1 - \frac{x^2+y^2}{R_1^2}}) + R_2(1 - \sqrt{1 - \frac{x^2+y^2}{R_2^2}}) \tag{A.23}$$

in which

$$\Delta_0 = \Delta_{01} + \Delta_{02} \tag{A.24}$$

By making the paraxial approximation for the beam passing through the lens, $\Delta(x, y)$ can be simplified:

$$\begin{aligned}\sqrt{1-\frac{x^2+y^2}{R_1^2}} &\cong 1-\frac{x^2+y^2}{2R_1^2}\\ \sqrt{1-\frac{x^2+y^2}{R_2^2}} &\cong 1-\frac{x^2+y^2}{2R_2^2}\end{aligned} \tag{A.25}$$

hence

$$\Delta(x,y) = \Delta_0 - \frac{x^2+y^2}{2}(\frac{1}{R_1}-\frac{1}{R_2}) \tag{A.26}$$

since the focal length f of the lens has a relation with R_1 and R_2 as:

$$\frac{1}{f} = (n-1)(\frac{1}{R_1}-\frac{1}{R_2}) \tag{A.27}$$

Consequently

$$\Delta(x,y) = \Delta_0 - \frac{x^2+y^2}{2f(n-1)} \tag{A.28}$$

Substituting $\Delta(x, y)$ into Eq. (A.19) and Eq. (A.18), the phase transform function becomes:

$$t(x,y) = e^{-ikn\Delta_0} e^{i\frac{k}{2f}(x^2+y^2)} \tag{A.29}$$

The phase transformation function $t(x, y)$ of the lens is used in Eq. (2.3) in Chapter 2. This equation can also be applied for other types of thin lens, e.g., the convex lens.

References

[1] H. Qassim, F. M. Miatto, J. P. Torres, M. J. Padgett, E. Karimi, and R. W. Boyd, "Limitations to the determination of a laguerre–gauss spectrum via projective, phase-flattening measurement," *JOSA B*, vol. 31, no. 6, pp. A20–A23, 2014.

[2] L. Allen, M. W. Beijersbergen, R. Spreeuw, and J. Woerdman, "Orbital angular momentum of light and the transformation of laguerre-gaussian laser modes," *Physical Review A*, vol. 45, no. 11, p. 8185, 1992.

[3] H. He, M. Friese, N. Heckenberg, and H. Rubinsztein-Dunlop, "Direct observation of transfer of angular momentum to absorptive particles from a laser beam with a phase singularity," *Physical Review Letters*, vol. 75, no. 5, p. 826, 1995.

[4] D. G. Grier, "A revolution in optical manipulation," *Nature*, vol. 424, no. 6950, p. 810, 2003.

[5] L. Torner, J. P. Torres, and S. Carrasco, "Digital spiral imaging," *Optics Express*, vol. 13, no. 3, pp. 873–881, 2005.

[6] G. C. Berkhout and M. W. Beijersbergen, "Method for probing the orbital angular momentum of optical vortices in electromagnetic waves from astronomical objects," *Physical Review Letters*, vol. 101, no. 10, p. 100801, 2008.

[7] M. Harwit, "Photon orbital angular momentum in astrophysics," *The Astrophysical Journal*, vol. 597, no. 2, p. 1266, 2003.

[8] M. Beijersbergen, R. Coerwinkel, M. Kristensen, and J. Woerdman, "Helical-

wavefront laser beams produced with a spiral phaseplate," *Optics Communications*, vol. 112, no. 5-6, pp. 321–327, 1994.

[9] L. Marrucci, C. Manzo, and D. Paparo, "Optical spin-to-orbital angular momentum conversion in inhomogeneous anisotropic media," *Physical Review Letters*, vol. 96, no. 16, p. 163905, 2006.

[10] N. Bent, H. Qassim, A. Tahir, D. Sych, G. Leuchs, L. Sánchez-Soto, E. Karimi, and R. Boyd, "Experimental realization of quantum tomography of photonic qudits via symmetric informationally complete positive operator-valued measures," *Physical Review X*, vol. 5, no. 4, p. 041006, 2015.

[11] D. N. Neshev, T. J. Alexander, E. A. Ostrovskaya, Y. S. Kivshar, H. Martin, I. Makasyuk, and Z. Chen, "Observation of discrete vortex solitons in optically induced photonic lattices," *Physical Review Letters*, vol. 92, no. 12, p. 123903, 2004.

[12] S. Feng and P. Kumar, "Spatial symmetry and conservation of orbital angular momentum in spontaneous parametric down-conversion," *Physical Review Letters*, vol. 101, no. 16, p. 163602, 2008.

[13] A. Mair, A. Vaziri, G. Weihs, and A. Zeilinger, "Entanglement of the orbital angular momentum states of photons," *Nature*, vol. 412, no. 6844, p. 313, 2001.

[14] Q.-F. Chen, B.-S. Shi, Y.-S. Zhang, and G.-C. Guo, "Entanglement of the orbital angular momentum states of the photon pairs generated in a hot atomic ensemble," *Physical Review A*, vol. 78, no. 5, p. 053810, 2008.

[15] R. Fickler, G. Campbell, B. Buchler, P. K. Lam, and A. Zeilinger, "Quantum entanglement of angular momentum states with quantum numbers up to 10,010," *Proceedings of the National Academy of Sciences*, vol. 113, no. 48, pp. 13642–13647, 2016.

[16] A. R. Altman, K. G. Köprülü, E. Corndorf, P. Kumar, and G. A. Barbosa, "Quantum imaging of nonlocal spatial correlations induced by orbital angular momentum," *Physical Review Letters*, vol. 94, no. 12, p. 123601, 2005.

[17] E. Nagali, L. Sansoni, F. Sciarrino, F. De Martini, L. Marrucci, B. Piccirillo, E. Karimi, and E. Santamato, "Optimal quantum cloning of orbital angular momentum photon qubits through hong–ou–mandel coalescence," *Nature Photonics*, vol. 3, no. 12, p. 720, 2009.

[18] J. Leach, B. Jack, J. Romero, A. K. Jha, A. M. Yao, S. Franke-Arnold, D. G. Ireland, R. W. Boyd, S. M. Barnett, and M. J. Padgett, "Quantum correlations in optical angle–orbital angular momentum variables," *Science*, vol. 329, no. 5992, pp. 662–665, 2010.

[19] M. Krenn, M. Huber, R. Fickler, R. Lapkiewicz, S. Ramelow, and A. Zeilinger, "Generation and confirmation of a (100× 100)-dimensional entangled quantum system," *Proceedings of the National Academy of Sciences*, p. 201402365, 2014.

[20] A. C. Dada, J. Leach, G. S. Buller, M. J. Padgett, and E. Andersson, "Experimental high-dimensional two-photon entanglement and violations of generalized bell inequalities," *Nature Physics*, vol. 7, no. 9, p. 677, 2011.

[21] D. Kaszlikowski, P. Gnaciński, M. Żukowski, W. Miklaszewski, and A. Zeilinger, "Violations of local realism by two entangled n-dimensional systems are stronger than for two qubits," *Physical Review Letters*, vol. 85, no. 21, p. 4418, 2000.

[22] T. Vértesi, S. Pironio, and N. Brunner, "Closing the detection loophole in bell experiments using qudits," *Physical Review Letters*, vol. 104, no. 6, p. 060401, 2010.

[23] R. W. Boyd, J. Leach, B. Jack, J. Romero, A. K. Jha, A. M. Yao, S. Franke-Arnold, D. G. Ireland, S. M. Barnett, and M. J. Padgett, "New twist on light beams for quantum information science," *Optics and Photonics News*, vol. 21, no. 12, pp. 48–48, 2010.

[24] J. C. García-Escartín and P. Chamorro-Posada, "Universal quantum computation with the orbital angular momentum of a single photon," *Journal of Optics*, vol. 13, no. 6, p. 064022, 2011.

[25] P. Zhang, B.-H. Liu, R.-F. Liu, H.-R. Li, F.-L. Li, and G.-C. Guo, "Implementation of one-dimensional quantum walks on spin-orbital angular momentum space of photons," *Physical Review A*, vol. 81, no. 5, p. 052322, 2010.

[26] S. K. Goyal, F. S. Roux, A. Forbes, and T. Konrad, "Implementing quantum walks using orbital angular momentum of classical light," *Physical Review Letters*, vol. 110, no. 26, p. 263602, 2013.

[27] P. Zhang, R.-F. Liu, Y.-F. Huang, H. Gao, and F.-L. Li, "Demonstration of deutschs algorithm on a stable linear optical quantum computer," *Physical Review A*, vol. 82, no. 6, p. 064302, 2010.

[28] A. De Oliveira, S. Walborn, and C. Monken, "Implementing the deutsch algorithm with polarization and transverse spatial modes," *Journal of Optics B: Quantum and Semiclassical Optics*, vol. 7, no. 9, p. 288, 2005.

[29] M. Cao, L. Han, R. Liu, H. Liu, D. Wei, P. Zhang, Y. Zhou, W. Guo, S. Zhang, H. Gao, *et al.*, "Deutschs algorithm with topological charges of optical vortices via non-degenerate four-wave mixing," *Optics Express*, vol. 20, no. 22, pp. 24263–24271, 2012.

[30] M. Cao, Y. Yu, L. Zhang, F. Ye, Y. Wang, D. Wei, P. Zhang, W. Guo, S. Zhang, H. Gao, *et al.*, "Demonstration of cnot gate with laguerre gaussian beams via four-wave mixing in atom vapor," *Optics Express*, vol. 22, no. 17, pp. 20177–20184, 2014.

[31] J. Wang, J.-Y. Yang, I. M. Fazal, N. Ahmed, Y. Yan, H. Huang, Y. Ren, Y. Yue, S. Dolinar, M. Tur, *et al.*, "Terabit free-space data transmission employing orbital angular momentum multiplexing," *Nature Photonics*, vol. 6, no. 7, p. 488, 2012.

[32] N. Bozinovic, Y. Yue, Y. Ren, M. Tur, P. Kristensen, H. Huang, A. E. Willner, and S. Ramachandran, "Terabit-scale orbital angular momentum mode division multiplexing in fibers," *Science*, vol. 340, no. 6140, pp. 1545–1548, 2013.

[33] S. Walborn, D. Lemelle, M. Almeida, and P. S. Ribeiro, "Quantum key distribution with higher-order alphabets using spatially encoded qudits," *Physical Review Letters*, vol. 96, no. 9, p. 090501, 2006.

[34] N. J. Cerf, M. Bourennane, A. Karlsson, and N. Gisin, "Security of quantum key distribution using d-level systems," *Physical Review Letters*, vol. 88, no. 12, p. 127902, 2002.

[35] S. Gröblacher, T. Jennewein, A. Vaziri, G. Weihs, and A. Zeilinger, "Experimental quantum cryptography with qutrits," *New Journal of Physics*, vol. 8, no. 5, p. 75, 2006.

[36] M. Mafu, A. Dudley, S. Goyal, D. Giovannini, M. McLaren, M. J. Padgett, T. Konrad, F. Petruccione, N. Lütkenhaus, and A. Forbes, "Higher-dimensional orbital-angular-momentum-based quantum key distribution with mutually unbiased bases," *Physical Review A*, vol. 88, no. 3, p. 032305, 2013.

[37] M. Mirhosseini, O. S. Magaña-Loaiza, M. N. OSullivan, B. Rodenburg, M. Malik, M. P. Lavery, M. J. Padgett, D. J. Gauthier, and R. W. Boyd, "High-dimensional quantum cryptography with twisted light," *New Journal of Physics*, vol. 17, no. 3, p. 033033, 2015.

[38] L. Zhu, A. Wang, J. Liu, J. Wang, C. Du, and Q. Mo, "Experimental demonstration of orbital angular momentum (oam) modes transmission in a 2.6 km conventional graded-index multimode fiber assisted by high efficient mode-group excitation," in *Optical Fiber Communication Conference*, pp. W2A–32, Optical Society of America, 2016.

[39] S. Chen and J. Wang, "Theoretical analyses on orbital angular momentum modes in conventional graded-index multimode fibre," *Scientific Reports*, vol. 7, no. 1, p. 3990, 2017.

[40] C. Paterson, "Atmospheric turbulence and orbital angular momentum of single photons for optical communication," *Physical Review Letters*, vol. 94, no. 15, p. 153901, 2005.

[41] M. Krenn, J. Handsteiner, M. Fink, R. Fickler, R. Ursin, M. Malik, and A. Zeilinger, "Twisted light transmission over 143 km," *Proceedings of the National Academy of Sciences*, vol. 113, no. 48, pp. 13648–13653, 2016.

[42] D. Cozzolino, D. Bacco, B. Da Lio, K. Ingerslev, Y. Ding, K. Dalgaard, P. Kristensen, M. Galili, K. Rottwitt, S. Ramachandran, *et al.*, "Fiber based high-dimensional quantum communication with twisted photons," *arXiv preprint arXiv:1803.10138*, 2018.

[43] H. Sosa-Martinez, N. Lysne, C. Baldwin, A. Kalev, I. Deutsch, and P. Jessen, "Experimental study of optimal measurements for quantum state tomography," *Physical Review Letters*, vol. 119, no. 15, p. 150401, 2017.

[44] K. Banaszek, G. Dariano, M. Paris, and M. Sacchi, "Maximum-likelihood estimation of the density matrix," *Physical Review A*, vol. 61, no. 1, p. 010304, 1999.

[45] F. Tonolini, S. Chan, M. Agnew, A. Lindsay, and J. Leach, "Reconstructing high-dimensional two-photon entangled states via compressive sensing," *Scientific Reports*, vol. 4, p. 6542, 2014.

[46] J. M. Renes, R. Blume-Kohout, A. J. Scott, and C. M. Caves, "Symmetric informationally complete quantum measurements," *Journal of Mathematical Physics*, vol. 45, no. 6, pp. 2171–2180, 2004.

[47] W. K. Wootters and B. D. Fields, "Optimal state-determination by mutually unbiased measurements," *Annals of Physics*, vol. 191, no. 2, pp. 363–381, 1989.

[48] A. J. Scott, "Tight informationally complete quantum measurements," *Journal of Physics A: Mathematical and General*, vol. 39, no. 43, p. 13507, 2006.

[49] A. M. Yao and M. J. Padgett, "Orbital angular momentum: origins, behavior and applications," *Advances in Optics and Photonics*, vol. 3, no. 2, pp. 161–204, 2011.

[50] M. Padgett and L. Allen, "Light with a twist in its tail," *Contemporary Physics*, vol. 41, no. 5, pp. 275–285, 2000.

[51] W. Ji, C.-H. Lee, P. Chen, W. Hu, Y. Ming, L. Zhang, T.-H. Lin, V. Chigrinov, and Y.-Q. Lu, "Meta-q-plate for complex beam shaping," *Scientific Reports*, vol. 6, p. 25528, 2016.

[52] L. Marrucci, "The q-plate and its future," *Journal of Nanophotonics*, vol. 7, no. 1, p. 078598, 2013.

[53] M. W. Beijersbergen, L. Allen, H. Van der Veen, and J. Woerdman, "Astigmatic laser mode converters and transfer of orbital angular momentum," *Optics Communications*, vol. 96, no. 1-3, pp. 123–132, 1993.

[54] N. González, G. Molina-Terriza, and J. P. Torres, "How a dove prism transforms the orbital angular momentum of a light beam," *Optics Express*, vol. 14, no. 20, pp. 9093–9102, 2006.

[55] M. Harris, C. Hill, P. Tapster, and J. Vaughan, "Laser modes with helical wave fronts," *Physical Review A*, vol. 49, no. 4, p. 3119, 1994.

[56] M. Padgett, J. Arlt, N. Simpson, and L. Allen, "An experiment to observe the intensity and phase structure of laguerre–gaussian laser modes," *American Journal of Physics*, vol. 64, no. 1, pp. 77–82, 1996.

[57] J. Leach, M. J. Padgett, S. M. Barnett, S. Franke-Arnold, and J. Courtial, "Measuring the orbital angular momentum of a single photon," *Physical Review Letters*, vol. 88, no. 25, p. 257901, 2002.

[58] X. Gu, M. Krenn, M. Erhard, and A. Zeilinger, "Gouy phase radial mode sorter for light: Concepts and experiments," *Physical Review Letters*, vol. 120, no. 10, p. 103601, 2018.

[59] Z. Zhang, Z. You, and D. Chu, "Fundamentals of phase-only liquid crystal on silicon (lcos) devices," *Light: Science & Applications*, vol. 3, no. 10, p. e213, 2014.

[60] N. Mukohzaka, N. Yoshida, H. Toyoda, Y. Kobayashi, and T. Hara, "Diffraction efficiency analysis of a parallel-aligned nematic-liquid-crystal spatial light modulator," *Applied Optics*, vol. 33, no. 14, pp. 2804–2811, 1994.

[61] H. Toyoda, T. Inoue, and T. Hara, "Application of liquid crystal on silicon spatial light modulator (lcos-slm) for manipulation and sensing," in *Information Optics (WIO), 2015 14th Workshop on*, pp. 1–3, IEEE, 2015.

[62] X. Zeng, J. Bai, C. Hou, and G. Yang, "Compact optical correlator based on one phase-only spatial light modulator," *Optics Letters*, vol. 36, no. 8, pp. 1383–1385, 2011.

[63] J. A. Davis, D. M. Cottrell, J. Campos, M. J. Yzuel, and I. Moreno, "Encoding amplitude information onto phase-only filters," *Applied Optics*, vol. 38, no. 23, pp. 5004–5013, 1999.

[64] E. Bolduc, N. Bent, E. Santamato, E. Karimi, and R. W. Boyd, "Exact solution to simultaneous intensity and phase encryption with a single phase-only hologram," *Optics Letters*, vol. 38, no. 18, pp. 3546–3549, 2013.

[65] J. C. Wyant and K. Creath, "Basic wavefront aberration theory for optical metrology," *Applied Optics and Optical Engineering*, vol. 11, no. part 2, pp. 28–39, 1992.

[66] R. Guenther, "Modern optics john wiley & sons," *Inc., New York*, 1990.

[67] P. P. Zupancic, "Dynamic holography and beamshaping using digital micromirror devices," *LMU Münich, Grainer Lab Harvard*, vol. 242, 2013.

[68] A. Jesacher, A. Schwaighofer, S. Fürhapter, C. Maurer, S. Bernet, and M. Ritsch-Marte, "Wavefront correction of spatial light modulators using an optical vortex image," *Optics Express*, vol. 15, no. 9, pp. 5801–5808, 2007.

[69] R. Dou and M. K. Giles, "Closed-loop adaptive-optics system with a liquid-crystal television as a phase retarder," *Optics Letters*, vol. 20, no. 14, pp. 1583–1585, 1995.

[70] R. Dou and M. K. Giles, "Phase measurement and compensation of a wave front using a twisted nematic liquid-crystal television," *Applied Optics*, vol. 35, no. 19, pp. 3647–3652, 1996.

[71] G. D. Love, "Wave-front correction and production of zernike modes with a liquid-crystal spatial light modulator," *Applied Optics*, vol. 36, no. 7, pp. 1517–1524, 1997.

[72] R. W. Bowman, A. J. Wright, and M. J. Padgett, "An slm-based shack–hartmann wavefront sensor for aberration correction in optical tweezers," *Journal of Optics*, vol. 12, no. 12, p. 124004, 2010.

[73] C. López-Quesada, J. Andilla, and E. Martín-Badosa, "Correction of aberration in holographic optical tweezers using a shack-hartmann sensor," *Applied Optics*, vol. 48, no. 6, pp. 1084–1090, 2009.

[74] T. Čižmár, M. Mazilu, and K. Dholakia, "In situ wavefront correction and its application to micromanipulation," *Nature Photonics*, vol. 4, no. 6, p. 388, 2010.

[75] A. Leszczyński and W. Wasilewski, "Calibration of wavefront distortion in light modulator setup by fourier analysis of multibeam interference," *JOSA A*, vol. 33, no. 4, pp. 683–688, 2016.

[76] P. Zupancic, P. M. Preiss, R. Ma, A. Lukin, M. E. Tai, M. Rispoli, R. Islam, and M. Greiner, "Ultra-precise holographic beam shaping for microscopic quantum control," *Optics Express*, vol. 24, no. 13, pp. 13881–13893, 2016.

[77] F. Bouchard, N. H. Valencia, F. Brandt, R. Fickler, M. Huber, and M. Malik, "Measuring azimuthal and radial modes of photons," *arXiv preprint arXiv:1808.03533*, 2018.

[78] J. Goodman, "Introduction to fourier optics," 2008.